The Pennsylvania State University
The Graduate School

DEVELOPMENT OF A VALIDATED DESIGN METHODOLOGY FOR VTOL SUAS

A Thesis in
Aerospace Engineering
by
Andrew P. Loughran

Submitted in Partial Fulfillment
of the Requirements
for the Degree of

Master of Science

May 2024

The thesis of Andrew P. Loughran was reviewed and approved by the following:

Julia A. Cole
Assistant Research Professor
Applied Research Laboratory
Thesis Co-Advisor

Simon W. Miller
Associate Professor of Aerospace Engineering
Applied Research Laboratory
Thesis Co-Advisor

Michael A. Yukish
Associate Professor of Aerospace Engineering
Head, Manufacturing Systems Division of the Applied Research Laboratory

Jack W. Langelaan
Professor of Aerospace Engineering
Director of Graduate Program

Abstract

There is growing interest in developing fixed-wing small unmanned aircraft systems (sUAS) with vertical takeoff and landing (VTOL) capabilities for many applications. To quickly and effectively design multiple configurations of VTOL sUAS such that the end product performs as intended, this thesis develops a validated, low-computational-cost design method. The design method incorporates a set of low-computational-cost weight and aero-propulsive performance models that were identified, selected, tuned, and validated through fabrication and flight testing of three different configurations of VTOL sUAS. An iterative design model approach was then developed to explore the design space to understand the trends between configurations in the mission space.

The Weight and Aero-propulsive models and methods are component-based weight build-up, low-order drag build-up, momentum theory propeller model, and an empirical approach to motor and electronic speed controller (ESC) efficiencies at relevant scales. Subcomponent models were validated by comparing them to the three VTOL sUAS configurations through flight testing in both hover and forward flight. Each vehicle's components were broken down by weight, compared against the design model's weight predictions, and found to be within 8.7% for all three configurations. Vehicle performance models for power draw in hover and forward flight were validated with measured power draw during flight testing in relevant conditions and were found to be within 13.1% of mean test data results for hover and 19.4% of mean test results for forward flight. Predictions were found to be most sensitive to the assumed motor, ESC, and propeller efficiencies, rotational velocity of motors, and accurate prediction of fuselage drag.

The validated subcomponent methods were then implemented in an iterative approach that required the convergence of the vehicle's gross weight and the battery weight. A mission space exploration was performed for a fixed-wing VTOL sUAS and a non-fixed-wing VTOL sUAS for comparison. These vehicles were under 55 lbs and it was determined that a maximum of 53 mile cruise for a 2-prop thrust vectoring sUAS and a maximum of 40 minute hover time for a quadrotor is possible. The mission space exploration found that there is a difference between the lightest vehicle and the most energy-efficient vehicle, which emphasizes that vehicle design objectives can vary the resultant vehicle design. In addition to a mission space exploration, this thesis presents a full conceptual design of a 2-prop thrust vectoring sUAS with an expected mission profile of 10 minute hover time and a 5 mile cruise distance with a gross weight of 2.28 pounds.

Table of Contents

List of Figures

List of Tables

List of Symbols

A_{rotor}	disk area of propeller
Æ_{wing}	wing aspect ratio
A_{mot}	cross-sectional area of motor
A_{prop}	cross-sectional area of propeller
a	speed of sound
BL	blade loading
b	wing span
C_D	three dimensional drag coefficient
$C_{D,\text{int}}$	interference drag coefficient
$C_{D,\text{wet}}$	skin friction drag coefficient
C_d	two dimensional drag coefficient
c_{do}	two dimensional profile drag coefficient
$C_{f,\text{fuse}}$	fuselage skin friction coefficient
C_L	three dimensional lift coefficient
C_l	two dimensional lift coefficient
$C_{P,\text{fwd}}$	three dimensional power coefficient
$C_{P,i,\text{fwd}}$	three dimensional induced power coefficient
$C_{T,\text{fwd}}$	three dimensional thrust coefficient
$\bar{c}$	average chord of wing
D	drag
DL	disk loading
d_{fuse}	fuselage diameter
d_{prop}	propeller diameter
E_{tot}	total energy
e	span efficiency
e_{wing}	Oswald's efficiency factor

F_{int}	drag interference multiplier
FF_{fuse}	fuselage form factor
f	fuselage area
g	acceleration of due to gravity
$g(\lambda_{\text{prop}})$	approximation function for profile coefficient
λ	taper ratio
λ_f	fuselage finesse ratio
λ_{prop}	inflow ratio of propeller
I	moment of inertia
J	advance ratio of propeller
κ	induced power factor
k	weight factor
l_{fuse}	fuselage length
Ma	Mach number
m_{motor}	Motor mass
n	rotational speed in revolutions per second
n_{blades}	number of blades
n_{motors}	number of motors
η_{esc}	ESC efficiency
η_{prop}	propeller efficiency
η_{mot}	motor efficiency
P	power
P_{elec}	electrical power
P_{FF}	forward flight power
P_{hover}	hover power
P_i	induced power
P_{mech}	mechanical or shaft power
P_o	profile power
P_{max}	maximum power
PD_{batt}	power density of battery
ρ	density of air
ρ_{CF}	density of carbon fiber
ρ_{foam}	density of foam

R_{fuse}	fuselage radius
R_{rotor}	propeller radius
R_{spar}	spar radius
Re_{fuse}	fuselage Reynolds number
c_{root}	wing root chord
SE_{batt}	specific energy of battery
S_{HT}	horizontal stabilizer area
S_{ref}	reference area of the fuselage
S_{VT}	vertical stabilizer area
S_{wet}	wetted surface area
S_{wing}	wing area
σ	blade solidity
$\sigma_{\text{y,CF}}$	flexural yield stress for carbon fiber
T_{rotor}	thrust per rotor
$T_{\text{rotor,fwd}}$	thrust per rotor in forward flight
$(T/W)_{\text{ideal}}$	ideal thrust-to-weight ratio
c_{tip}	wing tip chord
τ	torque
μ	advance ratio
V_{∞}	cruise speed
V_{tip}	propeller tip speed
$\cancel{V}_{\text{wing}}$	wing volume
v	dynamic viscosity
W	weight
w_{fuse}	fuselage width
ω	induced velocity at blade of propeller
Ω	propeller rotational speed in radians per second

Acknowledgments

I would like to take the time to acknowledge and thank those people who helped me complete my research project and thesis.

I would first like to thank Julia Cole for the opportunity to do research at the ARL and for helping me find my passion for Aerospace Engineering. In addition, thank you for being an amazing advisor both in my undergraduate studies and here at Penn State. I appreciate all the time spent helping me with my writing, research, and all the problems encountered along the way.

I would like to thank Simon Miller for his many insights and help for my research and thesis. I would also like to thank Mike Yukish for his thoughtful comments on this thesis.

I would like to thank Tori Lenze and Logan Hutton for the countless amazing hours in the bullpen and for help talking through many problems with research and graduate school. In addition, thank you for being great friends to enjoy the Penn State experience with.

I would like to thank Tom Jones both as a friend and for his vast knowledge of sUAS electronics, control, and piloting (expert-class ground-based pilot!) that supported me throughout my research.

Lastly, I would like to thank my family and friends for their unconditional support throughout my graduate studies.

This material is based on work funded by the Office of Naval Research through the Naval Sea Systems Command (NAVSEA) under Contract No. N000024-18-F-6401, Delivery Order 23F8402. The opinions, findings, conclusions, and recommendations expressed in this material are those of the authors and do not necessarily reflect the views of the Naval Sea Systems Command. Nor do they reflect the views of the Office of Naval Research or collaborators at the Naval Air Systems Command.

Chapter 1 Introduction

The overarching objective of this thesis is to enable the design of vertical takeoff and landing (VTOL) small unmanned aircraft systems (sUAS) through the development of a validated, low-computational-cost design methodology. Models for this design methodology include a component-based weight build-up, a low-order drag build-up, momentum theory, and a motor-ESC efficiency relation. These models were validated by comparing them to three different VTOL sUAS configurations through flight testing in both hover and forward flight. A condensed version of the design methodology flowchart is shown in Figure 1.1. This flowchart details where the information, model, data, or validation can be found for each portion of the design methodology in the thesis. Figure 1.1 can be used as a guide for this thesis and is similar to the complete flowchart for the proposed design methodology, which is shown in Figure 5.1. The resultant validated design methodology was used for a case study and mission space exploration between a fixed-wing VTOL sUAS and a non-fixed-wing VTOL sUAS, specifically a 2-prop thrust vectoring vehicle and a quadrotor. Lastly, a 2-prop thrust vectoring vehicle design is presented for a given reference mission.

This chapter provides an overview of the literature that relates to the research objective of developing a validated design methodology for vertical takeoff and landing (VTOL) small unmanned aircraft systems (sUAS). Current state-of-the-art design methods and functional aircraft systems in the scale and scope of this thesis are therefore reviewed. The motivation and background in Section 1.1 is split into four sections highlighting design objectives and parameters in Section 1.1.1, current designs and configurations in Section 1.1.2, existing design methodologies and models in Section 1.1.3, and techniques to validated models and methodologies in Section 1.1.4. Based on identified deficits in the current state-of-the-art, specific research objectives and questions are developed in Section 1.2.

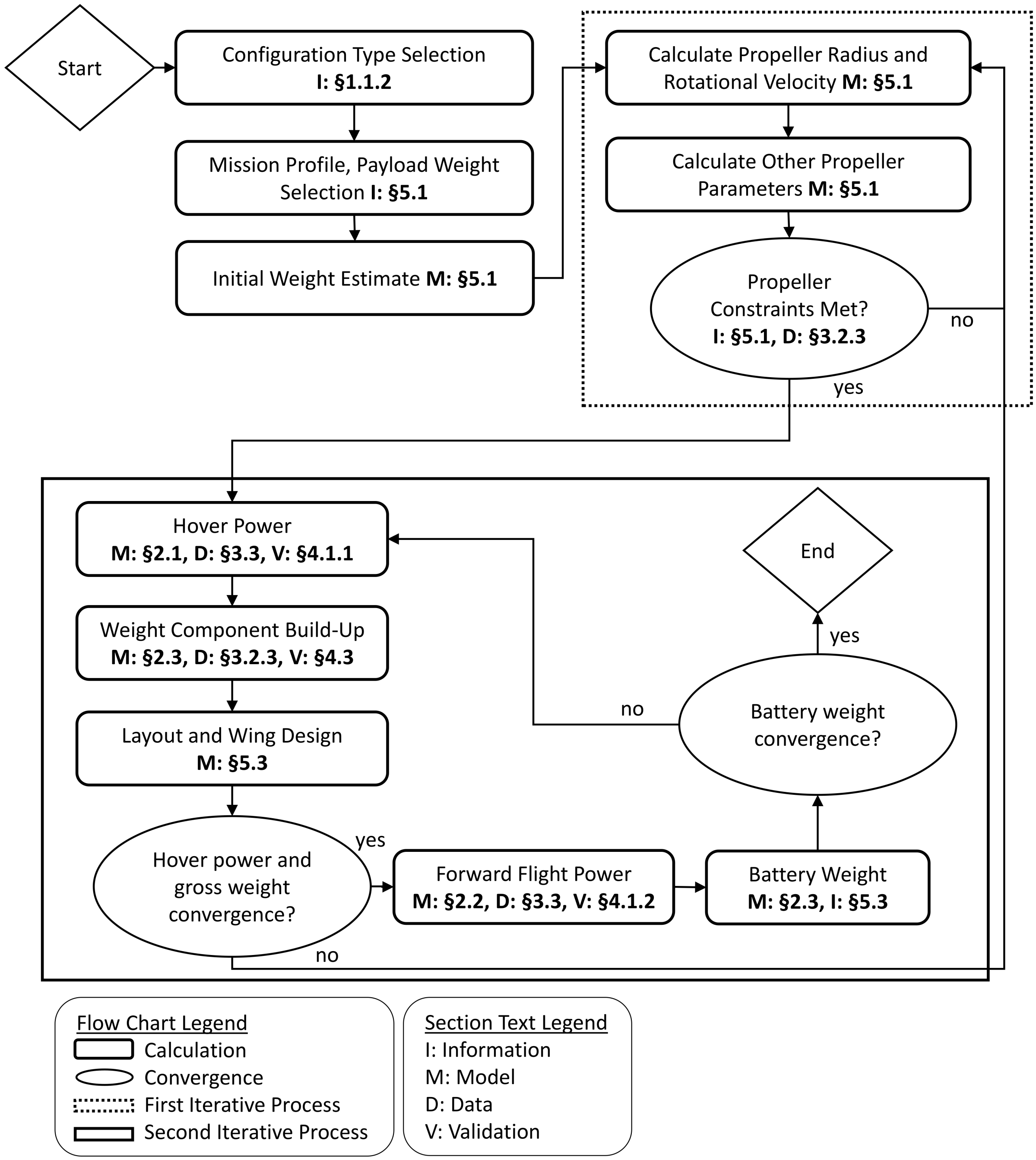

Figure 1.1: Condensed flowchart for the design methodology detailing where the information, model, data, or validation can be found in the thesis.

1.1 Motivation and Background

VTOL sUAS are between 1 and 55 pounds as dictated by FAA Part 107 sUAS regulations [1] and are known as Group 1 and 2 by the U.S. Department of Defense [2]. VTOL capabilities allow these vehicles to be runway-independent and are often achieved through a stable hover capability. Additionally, sUAS are portable based on their size and weight. VTOL sUAS features various configurations including those that rely on rotors only for lift in both hover and cruise (e.g., quadrotors) and those that feature fixed-wing lifting surfaces in cruise (e.g., tiltrotors and tiltwings). The latter tends to have better efficiency in cruise, while the former tends to have better efficiency in hover [3].

Because of the potential benefits of VTOL sUAS for many applications [4–6], having the ability to quickly design and quantitatively compare the mission performance of various configurations has value to the design community. Boundaries in the mission space where each configuration is optimal will aid decision-makers and so a design methodology with a common set of low-order design models must be developed. Validation of these models through flight test data is vital to ensure an accurate assessment of the design space.

1.1.1 Design Objectives and Parameters

When designing a VTOL sUAS, many design objectives and metrics are examined to determine which design is "best". The lightest vehicle can be desirable in cases where portability is a design driver [7, 8]. For missions that require significant range or endurance (e.g., Ref. [4–6, 8–11]), energy efficiency is paramount. Indoor operations [7] require significant maneuverability, while low-cost requirement [4, 5, 8, 11–13] may drive towards low-complexity solutions.

A vehicle's design objectives and parameters can vary based on the design reference mission. For example from Ref. [14], different conceptual vehicles were compared against each other based on five different design parameters (disk loading, total hover time, cruise speed, practical range, and flight time) and three different reference missions (urban, extra-urban, and long-range). Parameters and design objectives can be weighted and balanced depending on the vehicle configuration and mission to create the "best"vehicle design for VTOL sUAS. Another example could be the total endurance of the vehicle balanced against the total weight. Some negative effects of poor design objectives and parameters could include cost, maintenance, and an increased number of parts that could break [6, 8] or lead to excessive complexity.

Figure 1.2: Example of quadrotor VTOL sUAS from Hendrix et al. [17].

1.1.2 State of the Art Designs and Configurations

This section provides various examples of VTOL sUAS configurations and how each configuration is controlled along with each configuration's advantages and disadvantages to assist in the downselection of vehicle configurations for the proposed design methodology. Relating the vehicle configuration to the design metrics as in Section 1.1.1 is another step in downselecting. This will aid in identifying configurations for modeling in subsequent sections through careful examination of the complexity, control, and design considerations of each configuration.

Multirotor vehicles, like the common quadrotor configuration that has four propellers, use their propellers and motors for both the lift in hover and forward flight [15, 16]. This configuration is very popular because of its efficiency in hover; however, it does not have the same efficiency in forward flight as a fixed-wing vehicle [14]. An example of this configuration is shown in Figure 1.2.

Lift+cruise vehicle configurations, sometimes referred to as quadplanes, use separate propulsion systems for forward flight and hover. Forward flight propulsion is typically provided by one motor and propeller aligned axially with the oncoming flow while hover propulsion is typically provided by a quadrotor system [9, 10, 18]. Examples of this configuration can be seen in Figure 1.3. The main difference between the vehicles in Figure 1.3a and 1.3b is the use

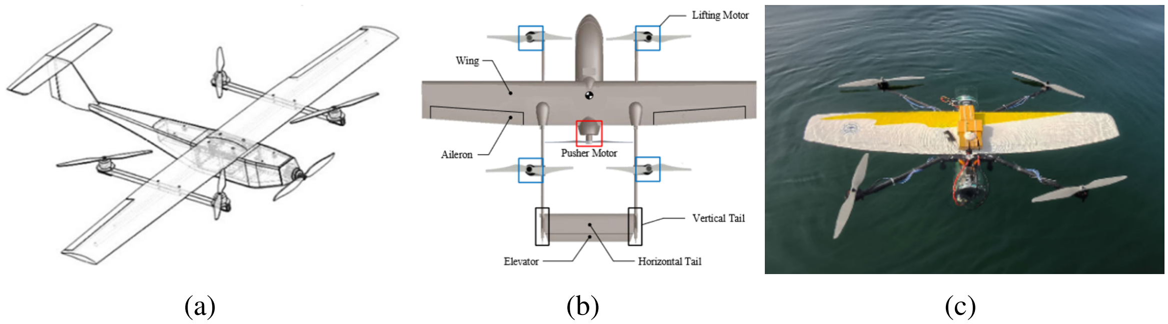

Figure 1.3: Examples of lift+cruise VTOL sUAS from (a) Dündar et al. [9], (b) Gu et al. [18], and (c) Lyu et al. [10].

of a pusher versus a tractor propeller. The vehicle in Figure 1.3c utilizes a tractor propeller vehicle that has operational capability in both water and air [10].

The control scheme for lift+cruise vehicle uses two entirely separate systems. In hover, roll, pitch, and yaw are controlled by differential thrust between the four motors. In forward flight, the four motors for hover are stopped and the control scheme is the same as a conventional fixed-wing aircraft [18]. Pitch is controlled by the elevator, roll control is achieved by the ailerons, and yaw control is produced by the rudder. During the transition phase between hover and forward flight, both the hover system and the forward flight system are active. One benefit of having separate control systems for hover and forward flight of lift+cruise configurations is that each can be optimized independently [10]. However, two *independent* propulsion systems has disadvantages such as the hover propulsion system adding drag in forward flight and the complexity and increased weight of the two systems for all flight domains.

Quadrotor tail-sitters are a quadrotor that has a wing surface to be used in forward flight. Examples of this configuration are shown in Figure 1.4. The vehicles in Figure 1.4b and 1.4c are similar except for the placement of the four propulsion systems. In hover, the vehicle is controlled by differential thrust between all four motors. In forward flight, the elevons control pitch and roll, yaw control is provided by differential thrust, and thrust is produced by the same motors and propellers in hover [5, 19]. The vehicle in Figure 1.4a is different from the other quadrotor tail-sitters because of how the vehicle produces differential thrust. This vehicle only has one motor onboard that provides power to all propellers evenly and at the same RPM — the thrust of each propeller is adjusted using variable pitch control [6].

One benefit of quadrotor tail-sitters is having both the ability to hover like a quadrotor and perform forward flight as a fixed-wing aircraft using the same propulsion system. This combined propulsion system saves weight and complexity compared to the lift+cruise. Further, having the wing parallel to the propeller axis allows for no penalty due to downwash in hover [6]. However,

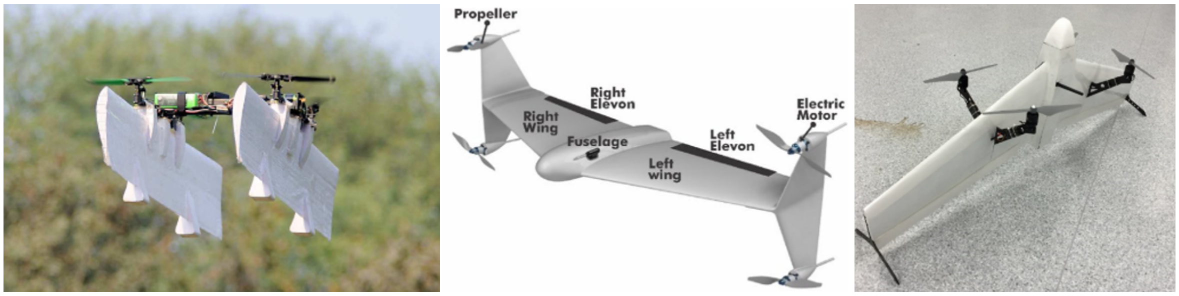

(a) (b) (c)

Figure 1.4: Examples of quadrotor tail-sitter VTOL sUAS from (a) Chipade et al. [6], (b) Priyambodo et al. [5], and (c) Wang et al. [8].

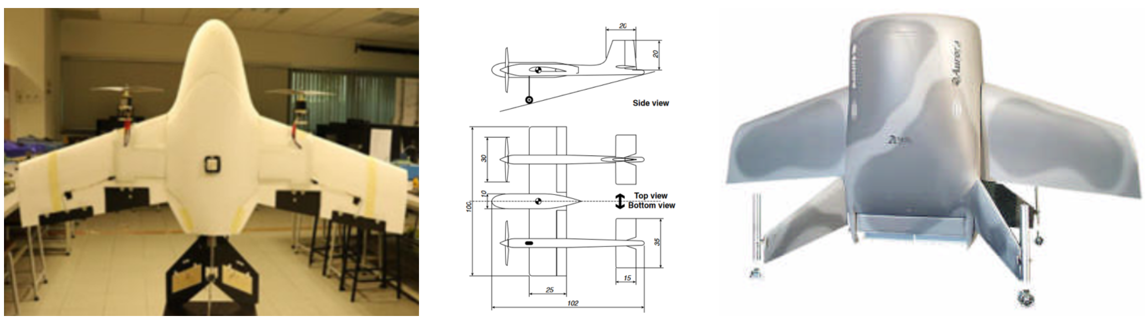

(a) (b) (c)

Figure 1.5: Examples of two and one prop tail-sitter VTOL sUAS from (a) Ke et al. [12], (b) Kubo and Suzuki [13], and (c) Schaefer and Baskett [20].

having one propulsion system does not allow for efficient optimization of the propulsion system for both static (hover) conditions and forward flight. The last drawback of a quadrotor tail-sitter is the tail structure needs to be larger to support the vehicle during landing which may increase vehicle weight that leads to decreased endurance and efficiency of the vehicle.

One (or two) propeller tail-sitters are a VTOL sUAS configuration that, while similar to a quadrotor tail-sitter, use a different number of propellers and the downstream effects on vehicle control. Examples of these vehicles can be seen in Figure 1.5. The main difference between the J-Lion (Figure 1.5a) and the vehicle in Figure 1.5b is the structure and placement of the tail. In both of these vehicles, elevons are used for control in hover but, for this approach to be effective, the control surfaces must be placed within the propeller wake [12, 13]. The GoldenEye (Figure 1.5c) is a single ducted fan vehicle that has two rows of control surfaces in the propeller's slipstream at the nozzle exit to control the vehicle [20].

A disadvantage of these one or two-propeller tail-sitters is the difficulty associated with maintaining control of the vehicle in the hover condition. All of the examples shown in

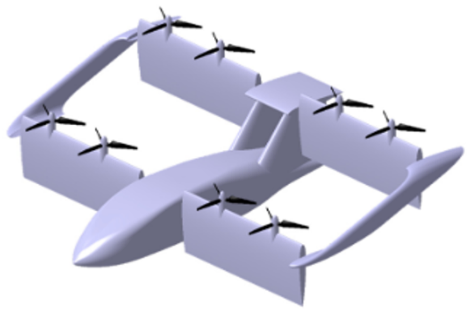

(a)

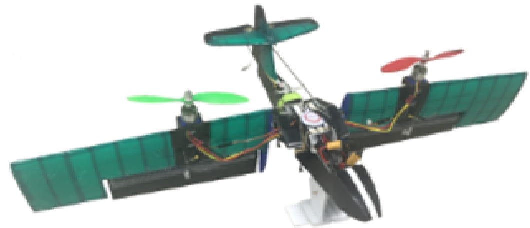

(b)

Figure 1.6: Examples of tilt-wing VTOL sUAS from (a) Palaia et al. [11] and (b) Sanchez-Revera et al. [21].

Figure 1.5 rely solely on control surfaces to hover in vertical flight. Control surface authority relies on non-zero flow conditions which means that, in hover, the control surfaces must operate in the wake of the propellers. Because of geometric constraints between the wing and propeller and limitations concerning propeller-induced velocities, gaining sufficient control authority can be challenging. Similar to quadrotor tail-sitters, the landing structure required is a disadvantage. An advantage of the configuration is that it requires only one or two motor-propeller systems, resulting in potential weight savings when compared with systems that require more (quadrotors, etc.)

Tilt-wing vehicles tilt their wings and integrated motor-propeller system to achieve hover and forward flight. Examples of tilt-wing vehicle configuration are shown in Figure 1.6. TiltOne (Figure 1.6a) incorporates eight propulsors, which are used in both hover and forward flight and are designed to have variable pitch propellers for efficiency in both forward flight and hover [11]. The vehicle in Figure 1.6b is a two-propeller tilt-wing vehicle that has been proven in flight testing. In hover, the wing and propulsion system tilt to provide control in pitch and yaw where differential thrust provides stability in roll [21]. In forward flight, both vehicles fly as conventional fixed-wing aircraft.

One benefit of tilt-wing vehicles is that control in hover, vertical flight, and transition can be accomplished straightforwardly through thrust vectoring. In addition, the prop-wash does not impinge on the wing because the prop wash and wing are aligned. A drawback of the configuration is that the mechanism weight required to controllably tilt the wing, propeller, and motor is more than that required to tilt a single propeller-motor system [22]. Transition can also be difficult in larger vehicles due to buffeting of the wing surface at high angles of attack [23].

Free-wing vehicles tilt their wings without a motor to achieve hover and forward flight. This is similar to the tilt-wing configuration, however free-wing vehicles have a zero-pitching

Figure 1.7: Free-wing vehicle in hover [24].

moment between the fuselage and the wing. An example of a free-wing configuration is shown in Figure 1.7. The free-wing configuration operates similarly to a tilt-wing configuration, but the tilt of the wing is accommodated by control surfaces on the wing [24].

Free-wing vehicles have most of the same benefits as tilt-wing vehicles. The one major benefit of free-wing vehicles over tilt-wing vehicles is decrease in weight from the lack of a required mechanism to control the tilt of the wing. This, however, comes with the drawback of increase complexity in control for VTOL missions [24].

Bi-copters are a vehicle configuration that are controlled entirely by two propellers with no fixed lifting surfaces; a configuration similar to a quadcopter but with only two motors. Figure 1.8 shows the Gemini bi-copter in hover controlled by a total of two servos and two motors. With the motion of the Gemini vehicle denoted by the arrow in Figure 1.8, the yaw and roll control is provided by thrust vectoring and pitch control via differential thrust, which is an effective means of achieving controllable flight [7].

The major advantage of the bi-copter configuration is its small profile in comparison with quadrotors. This allows for the vehicle to traverse through a thin horizontal space where other configurations could not. The complexity of the vehicle is low because there are only two motors and two servos. One disadvantage of a bi-copter configuration is its inefficiency in forward flight, similar to a quadrotor. Another disadvantage of this vehicle configuration is its scalability, as it has not been done before.

Tri-copter vehicle configurations are controlled by three propulsion systems that *could* have a lifting surface and typically have some sort of thrust vectoring to provide control in all three axes. Figure 1.9 shows an example of a tri-copter VTOL sUAS in both forward flight and hover

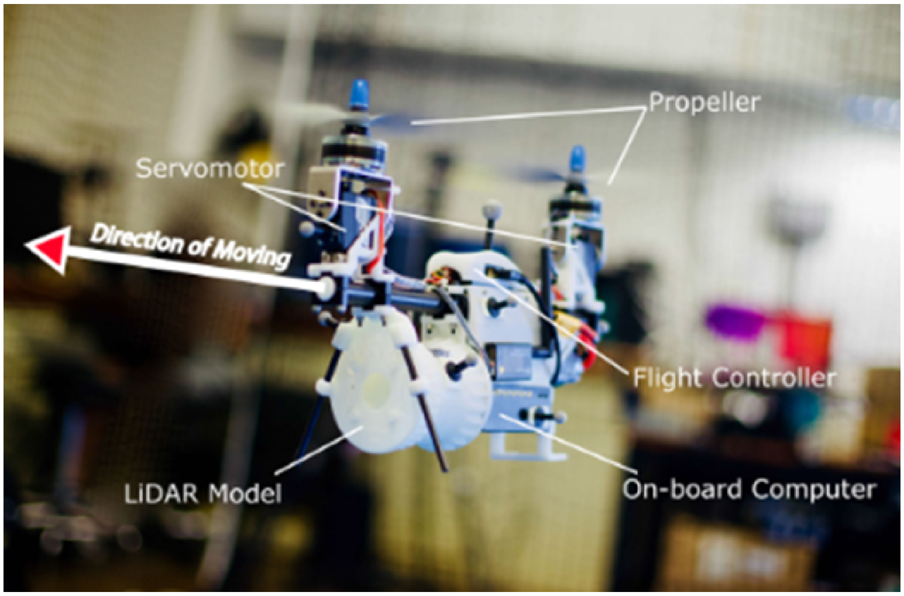

Figure 1.8: The Gemini bi-copter in hover [7].

orientations. This vehicle is a low-noise fully electrical platform that includes two tilt-motors in the front and a fixed and a coaxial ducted fan in the rear. This vehicle is a belly sitter, which means it lands and takes off from the bottom of the vehicle or wing, which is much different than the tail-sitter vehicles shown in Figures 1.4 and 1.5. In forward flight, only the front two tilt-motors are operating and providing thrust. In hover, the coaxial fans create 70-80% of the thrust needed, while the two front motors produce 10-30% of the thrust needed. Yaw control is accommodated in hover using the differential thrust of the coaxial motor, which induces a torque on the vehicle. Roll and pitch control is achieved by thrust differential [4].

One of the major benefits of tri-copters is the efficiency in hover and forward flight. Having the third motor in the back increases energy efficiency in hover, while not punishing the vehicle design with too much flying weight as compared to a quadrotor [4]. In the example of Figure 1.9, incorporating ducted fans has the benefit of low noise in hover [25]. With the coaxial motor submerged into the flying wing structure, there is no increase in drag from having a stopped propeller in forward flight. One of the drawbacks is the complexity of the system whereby having an inset coaxial ducted fan, two tilt-motors, and a flying wing is a very complex system. Another disadvantage is having the additional weight of a third motor.

A summary of VTOL sUAS configurations reviewed are compared in Pugh Matrices in Tables 1.1 and 1.2 to help downselect for configuration selection analysis. Table 1.1 highlights the advantages and disadvantages of each VTOL sUAS configuration where the positive indicates an advantage, the negative indicates a disadvantage, and a zero indicates that it is not

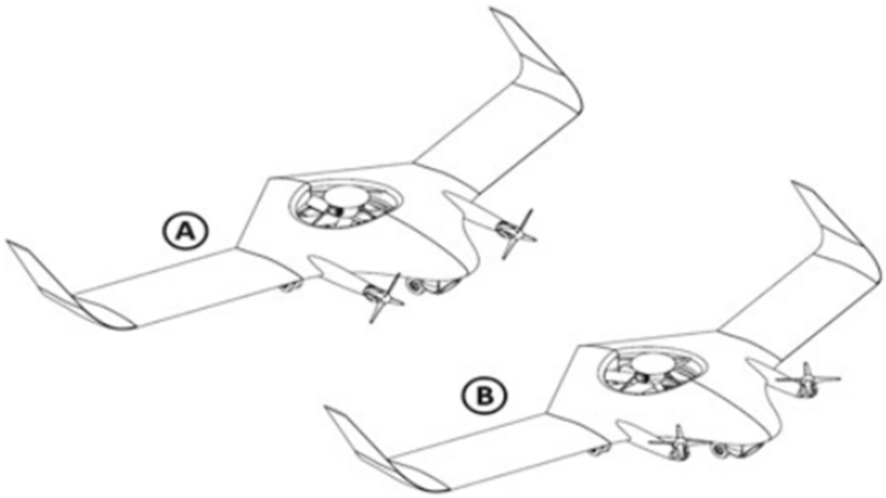

Figure 1.9: Example of a tri-copter VTOL sUAS from Ozdemir et al. [4].

Table 1.1: Summary of VTOL sUAS configurations' advantages and disadvantages.

+ : *advantage,* - : *disadvantage,* 0 : *neither or n/a*	Quad-rotor	Lift+ cruise	Quad-rotor Tail-sitter	One or Two Prop Tail-sitter	Tilt-wing	Free-wing	Bi-copter	Tri-copter
Maneuverability in Hover	+	+	+	0	0	0	-	+
Propulsion Complexity	0	-	0	+	+	+	-	0
Structural Complexity	0	-	-	0	-	-	+	0
Cost	0	-	-	+	0	+	0	0
Hover Efficiency	+	+	+	0	0	0	0	+
Forward Flight Efficiency	-	+	0	+	+	+	-	+

applicable or neither a disadvantage nor advantage. These advantages and disadvantages are related to the design objectives and parameters described in Section 1.1.1 and were considered when deciding the scores. Table 1.2 emphasizes the complexity of each configuration reviewed and the necessary component models required to evaluate each. With the information and criteria identified from Tables 1.1 and 1.2, the one or two prop tail-sitter and tri-copter have the least amount of disadvantages and the most amount of advantages which leads them to be downselected for future design configurations. The one or two-propeller tail-sitter is further downselected as it does not have downwash on its lifting surface and stopped edgewise propellers in forward flight.

Table 1.2: Summary of VTOL sUAS configurations' components to be modeled to predict performance.

	Quad-rotor	Lift+cruise	Quad-rotor Tail-sitter	One or Two Prop Tail-sitter	Tilt-wing	Free-wing	Bi-copter	Tri-copter
Axially oriented propellers in forward flight	no	yes	yes	yes	yes	yes	no	yes
Propellers in hover	yes	yes	yes	yes	yes	yes	yes	yes
Tangentially oriented propellers in forward flight	yes	no	no	no	no	no	yes	no
Stopped edgewise propellers in forward flight	no	yes	no	no	no	no	no	yes
Fixed-wing lifting surfaces	no	yes	yes	yes	yes	yes	no	yes
Streamlined fuselages	no	yes	yes	yes	yes	yes	yes	yes
External structural rod elements	yes	yes	yes	no	no	no	no	no
Propeller downwash on lifting surface	no	no	no	no	no	no	no	yes

1.1.3 Design Methodologies and Models

Many design methodologies have been developed for VTOL sUAS [23, 26] but few have flight test validation. Kamal and Ramirez-Serrano [23], for example, developed a design methodology for transitional VTOL sUAS in which the configuration is selected before the analysis phase through the application of structured design methods such as quality function deployment (QFD) and weighted Pugh methods. The approach was verified through a comparison of final performance estimations using other computational methods to the design requirements, but not through flight testing. Jae-Hyun et al. [26] investigated a sizing methodology for a lift+cruise hydrogen cell and battery vehicle. The approach suggested an iterative multi-mode constraint analysis with integrated propulsion system sizing, mission analysis, mass build-up, and optimization. A single 25 kg vehicle was conceptually designed using this approach and a previously developed computational method with a 10% maximum error on all of the designed vehicle parameters.

There are also a few studies that considered vehicles larger than VTOL sUAS (>55 lbs) that developed potentially applicable methodologies and models [14, 27–29]. For example, Kadiresan and Duffy [28] created a methodology to determine the best configuration for a given manned mission. The configurations examined were helicopters, multirotors, tiltrotors, tilt wings, and lift+cruise for a baseline mission of cruise and hover. Cole et al. [29] developed a methodology for configuration comparison of eVTOL vehicles for urban air mobility that identified the boundaries of the mission space where a conventional single-main-rotor helicopter is optimal and a lift-augmented compound helicopter is optimal based on varying technology assumptions.

Several design methodologies are used to design a specific VTOL sUAS vehicle configuration, however, none of those are a complete generic methodology [16, 30, 31]. Babetto and Stumpf [30] demonstrate a design methodology designs specifically for tiltrotor vehicles. Similarly, the eCalc [16] tool provides a simple hobbyist design platform where a UAV's parameters can be inputted for an output of performance and endurance. Unfortunately, the only VTOL sUAS that eCalc can handle is a quadrotor configuration. The last example is NDARC [32], which is typically used for full-scale VTOL design. Russell et al. [31] and Topper [33] used wind tunnel testing and hover test data to refine and validate NDARC for sUAS multirotors specifically.

Low-computational cost model techniques for VTOL sUAS have been explored in many studies [3, 6, 9, 21, 23, 26, 27, 34, 35]. So-called "rubber"modeling techniques, also known as empirical regressions can be used for individual component weight estimations, gross vehicle weight estimation, motor power estimation, and propeller revolution speed estimation [3, 9, 26, 27, 34] among other vehicle attributes. Another example is using momentum theory to calculate the hover power of a VTOL sUAS [9, 23, 26]. Blade element momentum theorem (BEMT) can calculate the thrust and drag of the propeller in multiple orientations [6]. Lifting line theory provides a low-cost modeling technique [6] for modeling forward flight lift and drag on wings. Lastly, an equivalent flat plate area can be used to calculate the drag of individual components of a vehicle in forward flight [6].

There are a few examples of high-computational cost methods that were used for VTOL sUAS that could apply to the proposed design methodology [6, 21]. The first example is using computer-aided design (CAD) and finite element method (FEM) to create a wing or other structural object on the vehicle [6]. Another example is using OpenVSP to perform computational fluid dynamics (CFD) on the entire vehicle, which is useful in getting the aerodynamic coefficients of the vehicle [21].

1.1.4 Design Model Validation

Review of existing studies provides examples of validated single configuration VTOL sUAS models and affords insight into validation techniques and methods to develop and validate empirical, semi-empirical, or higher fidelity models of a multiple VTOL sUAS configuration for this thesis. For example, Priyambodo et al. [5] used a vortex-lattice method supplemented with actuator disk theory for propellers to model a small VTOL quadrotor tail-sitter and compared it to flight test data. Wang et al. [8] developed an aerodynamic model of a quadrotor tail-sitter to design and fabricate a prototype vehicle. Ke et al. [12] designed and developed a novel thrust vectoring tail sitter called J-Lion and validated their model-based control method through flight testing.

Design models for VTOL sUAS are validated using a variety of techniques. Propulsion system performance predictions have been validated using thrust stands for static comparisons [6, 36, 37] and wind tunnel testing for dynamic comparisons [38]. Flight testing of VTOL sUAS has been used to validate empirical models [5] and flight controllers for controllability and autonomy [12, 21, 39]. Finally, another technique is to use an already validated model to validate a different model's results [5].

1.2 Research Objectives and Overview

The goal of this research is to develop a validated and generic design methodology for multiple configurations of VTOL sUAS. This goal will be accomplished by answering the following research questions:

1. Is it possible to use the same low-order methods to predict the performance of multiple VTOL sUAS configurations, and if so, which methods are most appropriate for this application?
2. How can these models be integrated into an automated, iterative design methodology that will produce a reasonable vehicle design?
3. What can the proposed design method reveal regarding the VTOL sUAS design space?

The answers to these research questions are addressed in this thesis as follows. A series of low-order models are described in Chapter 2. These models are downselected and validated through flight testing as described in Chapter 3 and Chapter 4. The validated models are incorporated into an automated, iterative design methodology as described in Chapter 5. Lastly, the design methodology was used for a mission space exploration and case study comparison between a quadrotor and 2-prop thrust vectoring vehicle as described in Chapter 6.

The work presented in this thesis is a continuation of already published work in AIAA SciTech 2024 "Design Model Validation for Small UAS VTOL using Flight Test Data" [40].

Chapter 2 Design Model

This chapter describes a series of low-order models identified for use within the proposed design methodology. Separate approaches were implemented to model hover, forward flight, and vehicle weight. The hover model is described in Section 2.1. The forward flight model is broken into five sections detailing lifting surface drag in Section 2.2.1, fuselage drag in Section 2.2.2, stopped propeller/motor drag Section 2.2.3, and combined drag and forward flight power for fixed-lifting surfaces vehicles and non-fixed-lifting surfaces vehicles in Section 2.2.4 and 2.2.5, respectively. The fuselage drag model is broken into five sub-sections identifying five models tested for VTOL sUAS. These five models are Hoerner's model in Section 2.2.2.1, Babetto's model in Section 2.2.2.2, Pollet's model in Section 2.2.2.3, Bacchini's model in Section 2.2.2.4, and Götten's model in Section 2.2.2.5. Lastly, the weight models are described in Section 2.3.

The approaches detailed in this chapter account for systems and interactions identified for the various VTOL sUAS configurations discussed in Table 1.2. Several methods discussed in Section 1.1.3 were selected for the design methodology as a compromise between low computational cost and the ability to capture relevant system performance.

2.1 Hover Model

The hover power is estimated using momentum theory [41]. The total hover power can be calculated by summing the induced power and the propeller's profile power. The induced power of the propeller can be calculated by

$$P_i = \kappa \frac{T_{\text{rotor}}^{3/2}}{\sqrt{2\rho A_{\text{rotor}}}} \tag{2.1}$$

where κ is the induced power factor, T_{rotor} is the thrust of a single propeller, ρ is the density of air, and A_{rotor} is the disk area of a single propeller. For these calculations, it was assumed that the thrust for a single propeller in hover is equal to the weight of the entire vehicle divided by the number of propellers. It was also assumed that the downwash on wing surfaces is negligible for the configurations modeled. The induced power factor is calculated according to Johnson [42] taking into account non-uniform inflow and miscellaneous induced losses as

$$\kappa = \frac{1.13}{1 - \frac{\sqrt{2C_T}}{n_{\text{blades}}}} \tag{2.2}$$

where C_T is the thrust coefficient and n_{blades} is the number of blades on the propeller. The profile power of the propeller is calculated from

$$P_o = \frac{1}{8}\sigma\rho c_{do} A_{\text{rotor}} \left(\Omega R_{\text{rotor}}\right)^3 \tag{2.3}$$

where σ is the solidity, c_{do} is the profile drag coefficient, and Ω is the rotational speed of the propeller in radians per second. For this thesis, the profile drag coefficient was assumed similar to an NACA 6612 airfoil at an appropriate Reynolds number using XFOIL [43]. This was assumed because of the propellers typically used for vehicles of this scale. Accurate hover power prediction is very sensitive to the assumed hover rotational speed of the propeller in revolutions per minute (RPM), which there is no current way to estimate without a specific motor-propeller combination. For the design model and validation in Chapter 4, RPM in hover was determined based on RPM versus thrust correlations found from thrust stand testing. For the developed design methodology, assumptions regarding the maximum tip speed based on the Mach number are used to estimate an initial RPM. Further explanation of the initial RPM estimate is discussed in Section 5.2.

The total hover power for a single propeller can be found using the equation from [41] as

$$P_{\text{hover}} = \frac{P_i + P_o}{\eta_{\text{mot}}\eta_{\text{esc}}} \tag{2.4}$$

where η_{mot} is the motor efficiency and η_{esc} is the electronic speed controller (ESC) efficiency. The total power in hover is the combination of the total hover power for each single propeller.

The motor-ESC efficiencies required for Equation 2.4 are calculated using a relation based on motor weight, as they were found to vary significantly from typically assumed values provided by manufacturers, e.g., 90-95% [26]. The variance from advertised 90-95% motor-ESC efficiencies is shown in Figure 2.1 for motor weights between 0.034 and 0.7 kilograms. To quantify this

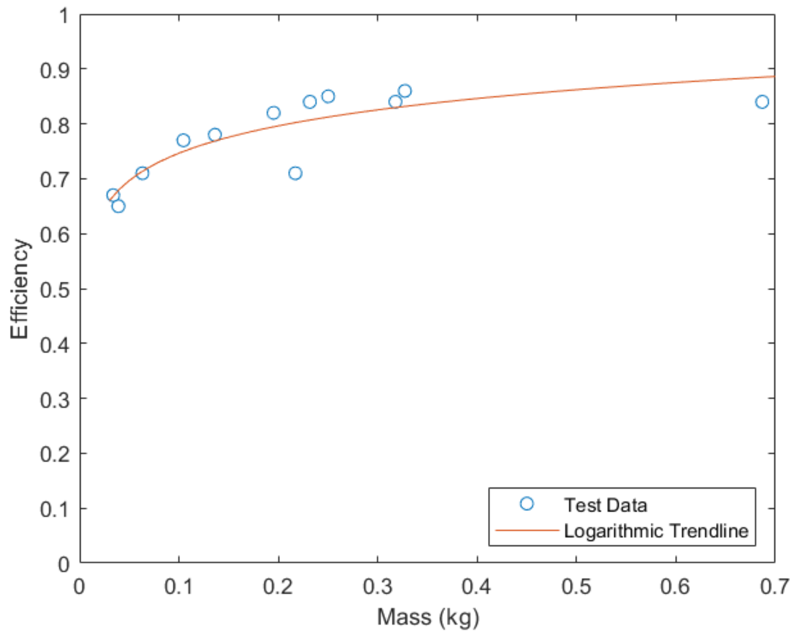

Figure 2.1: Efficiency as a function of motor mass in kilograms for motor and ESC tested with a logarithmic trend.

variation for the design method, a series of motors with appropriately matched ESCs were tested on a Tyto Robotics Series 1585 thrust and torque stand to measure efficiency similar to Gong et al. [36] and Green and McDonald [37]. The efficiency is defined as the ratio of the shaft power measured to the electric power (using a constant power supply) required by the motor-ESC system; data collected from the averaged maximum efficiency for each motor and propeller combination is shown in Figure 2.1. The resulting motor-ESC efficiency as a function of motor mass in kilograms (m_{mot}) is provided as

$$\eta_{\text{mot}}\eta_{\text{esc}} = 0.0718 \ln\left(\frac{m_{\text{motor}}}{1000}\right) + 0.4159 \tag{2.5}$$

This relationship is used directly in Equation 2.4 for the design method.

2.2 Forward Flight Model

For a fixed-winged vehicle in steady-level flight, the thrust required is equal to the drag of the vehicle. The power consumed by the vehicle is calculated as the power required by the motor-ESC-propeller system to provide the necessary thrust. Vehicle drag was estimated using a simple drag build-up approach [44] where the drag of each component was estimated and combined; effects of interference were accounted for using an empirical factor. Trim drag was neglected in this process.

2.2.1 Lifting Surface Drag

The drag of the wing, vertical stabilizer, and horizontal stabilizer are all calculated using a similar approach and equations. As such, only the calculations for wing drag are presented. The drag of the wing is given by

$$D_{\text{wing}} = \frac{1}{2}\rho V_\infty^2 S_{\text{wing}} \left(C_{D,\text{wing}} + \frac{C_{L,\text{wing}}^2}{\pi e \mathit{AR}_{\text{wing}}} \right) \tag{2.6}$$

where V_∞ is the airspeed, S_{wing} is the projected wing area, $\mathit{AR}_{\text{wing}}$ is the aspect ratio of the wing, $C_{D,\text{wing}}$ is the integrated profile drag coefficient of the wing, e is the span efficiency, and $C_{L,\text{wing}}$ is the lift coefficient of the wing assuming steady-level flight, i.e.,

$$C_{L,\text{wing}} = \frac{W_{\text{tot}}}{\frac{1}{2}\rho V_\infty^2 S_{\text{wing}}} \tag{2.7}$$

where W_{tot} is the total vehicle weight. The span efficiency and integrated profile drag are estimated using a numerical lifting line method supplemented with strip theory for local profile drag calculation based on Anderson [45].

To provide the most accurate estimate for the profile drag coefficient of the wing, the airfoil of the vehicle is analyzed over a range of Reynolds numbers based on the expected flight speed range of the vehicle. In this study, the lifting surface profile drag coefficient was found based on a 2-dimensional interpolation as a function of Reynolds number and lift coefficient. This relationship was developed based on results from an XFOIL analysis of a NACA 0015 airfoil with a Reynolds number ranging from 100,000 to 10,000,000 and a lift coefficient ranging from -0.5 to 1. The horizontal and vertical stabilizer profile drag is calculated assuming zero lift (neglecting trim drag) with a NACA 0009 airfoil at 50,000 Reynolds number. These NACA airfoils were selected as they are common for this scale of vehicles. It is important to note that this is a source of error for this approach however, as will be discussed in Chapter 4, the power required is dominated by the fuselage drag to a larger degree.

2.2.2 Fuselage Drag

Five approaches [14, 30, 35, 44, 46] for estimating the fuselage drag for VTOL sUAS in forward flight were considered and explored. The results of these models were compared with flight test data to select the most representative model for VTOL sUAS at this scale.

The fuselage Reynolds number and vehicle Mach number are required for several approaches. The Reynolds number of the fuselage is calculated as

$$Re_{\text{fuse}} = \frac{V_\infty l_{\text{fuse}}}{v} \tag{2.8}$$

where l_{fuse} is the length of the fuselage and v is the dynamic viscosity of air. The Mach number can be found using

$$Ma = \frac{V_\infty}{a} \tag{2.9}$$

where a is the speed of sound at standard sea level conditions.

2.2.2.1 Hoerner's Model

According to Hoerner [44], the fuselage drag coefficient is calculated as

$$C_{D,\text{fuse}} = \frac{0.45}{1/\lambda_f} + \frac{C_{D,\text{wet}}}{1 + (1/\lambda_f)^{3/2}} \left[3\lambda_f + 3\,(1/\lambda_f)^{1/2}\right] \tag{2.10}$$

where $C_{D,\text{wet}}$ is the skin friction drag coefficient and λ_f is the fineness ratio of the fuselage calculated as

$$\lambda_f = \frac{l_{\text{fuse}}}{d_{\text{fuse}}} \tag{2.11}$$

where l_{fuse} is the fuselage length and d_{fuse} is the fuselage diameter. The skin friction drag coefficient from Equation 2.10 was found using two-dimensional interpolation of streamlined-body empirical data found in Hoerner [44] based on the fineness ratio and Reynolds number of the fuselage. The drag of the fuselage can be calculated as

$$D_{\text{fuse}} = \frac{1}{2}\rho V_\infty^2 S_{\text{wet}} C_{D,\text{fuse}} \tag{2.12}$$

where S_{wet} is the wetted area of the fuselage. This can be estimated according to Hoerner [44] as

$$S_{\text{wet}} = 3 S_{\text{ref}} \frac{l_{\text{fuse}}}{d_{\text{fuse}}} \tag{2.13}$$

where S_{ref} is the reference area of the fuselage, which is the frontal cross-sectional area of the fuselage in this case.

2.2.2.2 Babetto's Model

In the approach of Babetto and Stumpf [30], fuselage area, f, is estimated as

$$f = kW_{\text{tot}}^{3/2} \tag{2.14}$$

where k is an empirical factor to account for Reynolds and Mach number. The equation for k changes based on a cutoff value for the Reynolds number due to the assumed transition of the flow as

$$k = \begin{cases} \dfrac{1.328}{\sqrt{Re_{\text{fuse}}}} & Re_{\text{fuse}} < 5 \times 10^5 \\ \dfrac{0.455}{\left(\log_{10} Re_{\text{fuse}}\right)^{2.58} \left(1 + 0.144Ma^2\right)^{0.65}} & Re_{\text{fuse}} \geq 5 \times 10^5 \end{cases} \tag{2.15}$$

The drag of the fuselage is found using

$$D_{\text{fuse}} = \frac{1}{2}\rho V_\infty^2 f \quad . \tag{2.16}$$

It is noteworthy that this approach does not take into account the actual fuselage geometry, instead making assumptions based on the vehicle's gross weight. While this is expected to be less accurate, it allows for estimations without the need for the details of the fuselage, which may be unknown early in the design process.

2.2.2.3 Pollet's Model

The third approach from Pollet et al. [35] estimates the fuselage drag coefficient as

$$C_{D,\text{fuse}} = C_{f,\text{fuse}} FF_{\text{fuse}} \frac{S_{\text{wet,fuse}}}{S_{\text{ref,fuse}}} \tag{2.17}$$

where C_f is the skin friction coefficient and FF is the fuselage form factor. The skin friction coefficient is found using

$$C_{f,\text{fuse}} = \frac{0.455}{\left(\log_{10} Re_{\text{fuse}}\right)^{2.58} \left(1 + 0.144Ma^2\right)^{0.65}} \tag{2.18}$$

Equation 2.18 is similar to Equation 2.15, however, there is no Reynolds number effect incorporated into Pollet's model. The form factor for the fuselage is given as

$$FF_{\text{fuse}} = 1 + \frac{60}{\lambda_f^3} + \frac{\lambda_f}{400} \quad . \tag{2.19}$$

The wetted surface area for the fuselage is estimated as

$$S_{\text{wet,fuse}} = \pi d_{\text{fuse}} l_{\text{fuse}} \left(1 - \frac{2}{\lambda_f}\right)^{2/3} \left(1 + \frac{1}{\lambda_f^2}\right) \quad . \tag{2.20}$$

The drag of the fuselage can then be found using

$$D_{\text{fuse}} = \frac{1}{2}\rho V_\infty^2 S_{\text{wet,fuse}} C_{D,\text{fuse}} \tag{2.21}$$

2.2.2.4 Bacchini's Model

The fourth approach from Bacchini and Crestino [14] is very similar to Pollet's method, however, there are some minor differences in calculating skin friction and form factor for the fuselage. The skin friction drag coefficient is calculated using

$$C_{f,\text{fuse}} = \frac{1.328}{\sqrt{Re_{\text{fuse}}}} \tag{2.22}$$

Equation 2.22 is similar to Equation 2.15, however, there is no Reynolds number effect incorporated into Bacchini's model. The form factor of the fuselage is calculated as

$$FF_{\text{fuse}} = 1 + 2.2\left(\frac{1}{\lambda_f}\right)^{3/2} - 0.9\left(\frac{1}{\lambda_f}\right)^3 \quad . \tag{2.23}$$

Using Equation 2.17 and 2.21, the drag of the fuselage can be calculated.

2.2.2.5 Götten's Model

The last model comes from Götten et al. [46]. It is very similar to Bacchini's model [14] with a modification to the fuselage form factor. The fuselage form factor in this model is found with the following equation

$$FF_{\text{fuse}} = cs_1 \lambda_f^{cs_2} + cs_3 \tag{2.24}$$

where cs_1, cs_2, and cs_3 are found with the following equations

$$cs_1 = -0.825885 \left(\frac{2R_{\text{fuse}}}{w_{\text{fuse}}}\right)^{0.411795} + 4.0001 \tag{2.25}$$

$$cs_2 = -0.340977 \left(\frac{2R_{\text{fuse}}}{w_{\text{fuse}}}\right)^{7.54327} - 2.27920 \tag{2.26}$$

$$cs_3 = -0.013846 \left(\frac{2R_{\text{fuse}}}{w_{\text{fuse}}}\right)^{1.34253} + 1.11029, \tag{2.27}$$

respectively; w_{fuse} is the fuselage width.

2.2.3 Stopped Propeller/Motor Drag

Two drag terms are included to account for any vertically aligned motor and propellers that do not tilt to provide thrust in forward flight (stopped propellers). The motor is conservatively treated as a cylinder in the streamwise direction at the appropriate Reynolds number dictated by the flight speed. The drag of the motor is

$$D_{\text{mot}} = \frac{1}{2}\rho V_\infty^2 A_{\text{mot}} C_{D,\text{cylinder}} \tag{2.28}$$

where A_{mot} is the cross-sectional area of the motor and $C_{D,\text{cylinder}}$ is the drag coefficient of a cylinder. The drag of a propeller that is idle in forward flight is found using the following equation

$$D_{\text{prop}} = \frac{1}{2}\rho V_\infty^2 A_{\text{prop}} C_{D,\text{prop}} \tag{2.29}$$

where A_{prop} is the cross-sectional area of the propeller and $C_{D,\text{prop}}$ is the drag coefficient of the propeller that is horizontal in forward flight. The cross-sectional area of the propeller is not the disk area, but the side-ways area perpendicular to the airflow. The drag coefficient of the propeller is calculated from [35] as

$$C_{D,\text{prop}} = 0.1\sigma \quad . \tag{2.30}$$

2.2.4 Combined Drag and Forward Flight Power for Vehicles with Fixed-Lifting Surfaces

The total drag of the vehicle is the sum of the individual components drag relevant to the configuration with an assumed interference drag multiplier of F_{int}. For example, for a lift+cruise configuration, which has a fuselage, wing, vertical and horizontal stabilizers, and stopped motors and propellers in forward flight, the total drag could be calculated

$$D_{\text{tot}} = F_{\text{int}} \left(D_{\text{fuse}} + D_{\text{wing}} + D_{HT} + D_{VT} + D_{\text{mot}} + D_{\text{prop}} \right) \tag{2.31}$$

where D_{HT} and D_{VT} are the drag of the horizontal and vertical stabilizer, respectively. The interference drag multiplier, F_{int}, was assumed to be 10% [3] to account for the drag between individual components.

Lastly, the total power to achieve forward flight for this model is the drag multiplied by the airspeed of the vehicle, V_∞, divided by the propeller efficiency, η_{prop}, and the combined motor-ESC efficiency as discussed in Section 2.1, i.e.,

$$P_{FF} = \frac{V_\infty D_{\text{tot}}}{\eta_{\text{mot}} \eta_{\text{esc}} \eta_{\text{prop}}} \quad . \tag{2.32}$$

The motor-ESC efficiency for forward flight is assumed to be the same as calculated using Equation 2.5 in hover. Inherently, this assumes that the motor, ESC, and propeller are well-matched and that their maximum efficiency in static torque-RPM conditions does not vary significantly from their maximum efficiency in forward flight torque-RPM conditions. The propeller efficiency in forward flight, η_{prop}, is calculated based on a method from McCormick [47], i.e.,

$$\eta_{\text{prop}} = \frac{C_{T,\text{fwd}} J}{C_{P,\text{fwd}}} \tag{2.33}$$

where $C_{T,\text{fwd}}$ is the thrust coefficient in forward flight, J is the advance ratio of the propeller, and $C_{P,\text{fwd}}$ is the power coefficient in forward flight. The advance ratio is calculated as

$$J = \frac{V_\infty}{2 n R_{\text{rotor}}} \tag{2.34}$$

where n is the rotational speed of the propeller in revolutions per second. The thrust coefficient in forward flight is calculated as

$$C_{T,\text{fwd}} = \frac{T_{\text{rotor,fwd}}}{\rho n^2 \left(2 R_{\text{rotor}} \right)^4} \tag{2.35}$$

where $T_{\text{rotor,fwd}}$ is the thrust per rotor in forward flight, which is equal to the total drag calculated in Equation 2.31 divided by the number of rotors. The power coefficient in forward flight is calculated as

$$C_{P,\text{fwd}} = C_{T,\text{fwd}} J + C_{P,i,\text{fwd}} + \frac{\pi^4 \sigma c_{do} g(\lambda_{\text{prop}})}{32} \tag{2.36}$$

where $C_{P,i,\text{fwd}}$ is the induced power coefficient in forward flight and $g(\lambda_{\text{prop}})$ is the approximation function for profile coefficient, which is calculated based on propeller inflow ratio, λ_{prop}, as

$$g(\lambda_{\text{prop}}) = \frac{1}{2}\left[\left(1+\lambda_{\text{prop}}^2\right)^{1/2}\left(2+\lambda_{\text{prop}}^2\right) - \lambda_{\text{prop}}^4 \log\left(\frac{1+\sqrt{1+\lambda_{\text{prop}}^2}}{\lambda_{\text{prop}}}\right)\right] \tag{2.37}$$

and

$$\lambda_{\text{prop}} = \frac{V_\infty}{\Omega R_{\text{rotor}}} \quad . \tag{2.38}$$

The induced power coefficient is calculated as

$$C_{P,i,\text{fwd}} = \frac{1.12 C_{T,\text{fwd}}\omega}{2nR_{\text{rotor}}} \tag{2.39}$$

where ω is the induced velocity at the blade of the propeller and is calculated as

$$\omega = \frac{1}{2}\left[-V_\infty + \sqrt{V_\infty^2 + \left(\frac{2T_{\text{rotor,fwd}}}{\rho A_{\text{rotor}}}\right)}\right] \quad . \tag{2.40}$$

2.2.5 Combined Drag and Forward Flight Power for Vehicles Without Fixed-Lifting Surfaces

The combined drag and forward flight power is different for vehicles without fixed-lifting surfaces. Quadrotor vehicles are vehicles without fixed-lifting surfaces and rely on their propellers for lift in forward flight. The total vehicle's power in forward flight for vehicles without fixed-lifting surfaces can be calculated as

$$P_{FF} = \frac{P_P + P_{\text{rotors}}}{\eta_{\text{mot}}\eta_{\text{esc}}} \tag{2.41}$$

where P_P is the parasite power and P_{rotors} is the power from the rotors in forward flight, which is calculated using

$$P_{\text{rotors}} = n_{\text{rotors}}(P_{\text{o,fwd}} + P_{i,\text{fwd}}) \tag{2.42}$$

where $P_{\text{o,fwd}}$ is the profile power in forward flight and $P_{i,\text{fwd}}$ is the induced power in forward flight. The profile power and the induced power in forward flight for an individual propeller are calculated from Leishman [41] as

$$P_{\text{o,fwd}} = (1 + 4.3J)P_{\text{o,hover}} \tag{2.43}$$

$$P_{i,\mathrm{fwd}} = \frac{\kappa\, T_{\mathrm{rotor}}^2}{2\rho A_{\mathrm{rotor}} V_\infty} \quad , \tag{2.44}$$

respectively. $P_{\mathrm{o,hover}}$ is found using Equation 2.3 and κ is the induced power factor. T_{rotor} is the thrust per rotor and, for these vehicles, is the total weight of the vehicle and the drag of the vehicle divided by the total number of propellers. Lastly, from Equation 2.41, P_P is calculated using

$$P_P = V_\infty D_{\mathrm{tot}} \tag{2.45}$$

where D_{tot} is the total drag and is found using the relationships presented in Carroll et al. [48] for quadrotors.

2.3 Weight Models

The weight model combines empirical and semi-empirical estimations for the weight of each sub-component of the vehicles. Although the list of relevant sub-components varies by configuration, as seen in Table 1.2, the full set of models includes the propellers, motors, ESCs, batteries, fuselages, wings, empennages, transition mechanisms, and avionics. The units of these equations are metric unless otherwise noted, with all weights provided in Newtons.

The first sub-component is the propellers whose weight can be calculated as

$$W_{\mathrm{props}} = \begin{cases} n_{\mathrm{motors}} 0.0884\, d_{\mathrm{prop}}^{1.5113} g & d_{\mathrm{prop}} \leq 0.254 \\ n_{\mathrm{motors}} \left(0.0879\, d_{\mathrm{prop}} - 0.0044\right) g & d_{\mathrm{prop}} > 0.254 \end{cases} \tag{2.46}$$

where d_{prop} is the diameter of the propeller in meters, g is the acceleration of gravity, and n_{motors} is the number of motors or propellers. The relations for these equations are derived from an online database of recorded propeller diameters and weights [49].

The motor, ESC, and battery weights are calculated using relations based on the maximum power required for flight. The maximum power required for flight per propeller is driven by the power required to perform vertical takeoff and is calculated as

$$P_{\max} = \frac{\left(\frac{T}{W}\right)_{\mathrm{ideal}} P_{\mathrm{hover}}}{\eta_{\mathrm{mot}} \eta_{\mathrm{esc}}} \tag{2.47}$$

where $\left(\frac{T}{W}\right)_{\mathrm{ideal}}$ is the ideal thrust-to-weight ratio. The ideal thrust-to-weight ratio is assumed to be 1.5 following the work of Kamal and Ramirez-Serrano [23]. The hover power is used rather than the forward flight power for this sizing as it is the driving design case.

With the maximum power expected in flight, the combined weight of all motors is calculated according to [26] as

$$W_{\text{motors}} = \frac{n_{\text{motors}} g}{1000} \left(0.196 \times 10^{-5} P_{\max}^2 + 0.201 P_{\max} + 5.772\right) \tag{2.48}$$

and the ESC weight is calculated according to [30] as

$$W_{\text{escs}} = \frac{n_{\text{motors}} g}{1000} \left(0.0654 P_{\max}\right) \quad . \tag{2.49}$$

The battery weight is calculated as the maximum weight required based on either energy capacity or maximum power draw, i.e.,

$$W_{\text{batt}} = \max\left(\frac{E_{\text{tot}}}{SE_{\text{batt}}}, \frac{P_{\max}}{\eta_{\text{mot}} \eta_{\text{esc}} PD_{\text{batt}}}\right) \tag{2.50}$$

where SE_{batt} and PD_{batt} are the specific energy and the power density of the battery, respectively. These values will depend on the battery type's chemistry and cell configuration. In this analysis, the battery-specific energy and battery power density are based on lithium polymer (LiPo) batteries [50].

The next sub-component weight model is for the fuselage, which is calculated as a percentage of the total weight as [30]

$$W_{\text{fuse}} = 0.09 W_{\text{tot}} \quad . \tag{2.51}$$

Since fuselage weight is both a fraction of and a part of the total weight, the weight models need to be iterated on within the design methodology and will be discussed in more detail in Section 6.2.

The wing weight is calculated based on an assumed semi-monocoque fabrication approach including foam and spars. The spar weight, W_{spar}, is calculated by treating the spar as a carbon tube cantilevered beam under a 5 G wingtip load as

$$W_{\text{spar}} = \frac{\rho_{\text{CF}} g b \pi}{2} \left(R_{\text{spar,outer}}^2 - R_{\text{spar,inner}}^2\right) \tag{2.52}$$

where $R_{\text{spar,outer}}$ is the outer radius of the spar, which for a winged vehicle is assumed to be half of the wing's thickness, ρ_{CF} is the density of carbon fiber, b is the wing span, and $R_{\text{spar,inner}}$ is the inner radius of the spar, which is calculated using

$$R_{\text{spar,inner}} = \left(\frac{R_{\text{spar,inner}}^4 - 4I}{\pi}\right)^{\frac{1}{4}} \tag{2.53}$$

where I is the moment of inertia and is calculated as

$$I = \frac{W_{\text{tot}} n_{\text{load}} b R_{\text{spar,outer}}}{4\sigma_{\text{y,CF}}} \tag{2.54}$$

where n_{load} is the load factor of 5 and $\sigma_{\text{y,CF}}$ is the flexural yield stress for carbon fiber tubes. This is an example for a winged vehicle, however, the calculation for a non-winged vehicle, e.g., a quadrotor, is quite similar. The foam weight is calculated roughly as

$$W_{\text{foam}} = \rho_{\text{foam}} g \cancel{V}_{\text{wing}} \tag{2.55}$$

where ρ_{foam} is the density of the foam, which is assumed to be 72 $^{\text{kg}}/_{\text{m}^3}$ [51]. $\cancel{V}_{\text{wing}}$ is the volume of the wing and is calculated by the cross-sectional area of a NACA 0015 airfoil [52] multiplied by the wing span as shown

$$\cancel{V}_{\text{wing}} = 0.10267\bar{c}^2 b \tag{2.56}$$

where $\bar{c}$ is the average chord of the wing. The total weight of the wing is

$$W_{\text{wing}} = W_{\text{foam}} + W_{\text{spar}} \quad . \tag{2.57}$$

The last two components used for the design model are the transition mechanism weight and the avionics weight. There was no relation found for either component within the literature, so both components are calculated using a percentage based on the total weight of the vehicle. These percentages are an average of the vehicles built and tested for this work and as described in Chapter 3. The transition mechanism refers to the mechanism that is responsible for tilting the propulsion system to a desired angle. The weight of this mechanism can be approximated as

$$W_{\text{transition}} = 0.06\left(W_{\text{tot}} - W_{\text{batt}}\right) \quad . \tag{2.58}$$

Similarly, the avionics weight is approximated as

$$W_{\text{avionics}} = 0.22\left(W_{\text{tot}} - W_{\text{batt}}\right) \quad . \tag{2.59}$$

The total weight of the vehicle can be calculated as the sum of relevant subcomponent models.

Chapter 3 Experimental Methods

This chapter describes the experimental methods used to

1. Identify the motor-ESC efficiencies
2. Downselect to an appropriate fuselage model
3. Develop appropriate weight models
4. Validate general trends in predicted vehicle performance for three different VTOL sUAS configurations

Motor-ESC efficiencies were found using a thrust stand as described in Section 3.1. Items 2, 3, and 4 required the selection, configuration, and assessment of functional functional VTOL sUAS. These vehicles are described in Section 3.2 and also the weight breakdowns are provided. The 3rd and 4th items were accomplished using the results of flight testing each vehicle as described in Section 3.3.

3.1 Motor Efficiency Testing

An experiment was run to determine a trend between motor weight and combined motor and ESC efficiency. This experiment was performed because the efficiencies between measured efficiencies and manufacturer-claimed efficiencies varied. The experiment involved a range of 12 different motors with a consistent ESC run on a Tyto Robotics Series 1585 Thrust Stand. The variables recorded during this experiment were electrical power draw, thrust, RPM, and torque. The power draw is measured through the data acquisition board and a constant power supply. The thrust and torque are measured using three separate strain gauges. The RPM was measured using an optical probe mounted and adjusted to be near the motor. The setup of the system and the key components are shown in Figure 3.1. The motors and propeller combinations used for thrust stand testing are listed in Table 3.1.

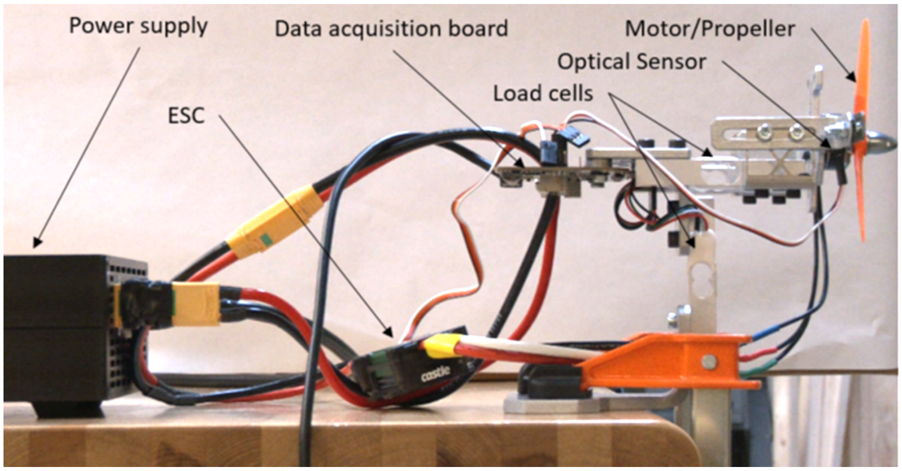

Figure 3.1: Experimental setup for motor efficiency testing with key components marked.

Table 3.1: Summary of motor and propeller combinations for thrust stand testing.

Motor	Propeller	Weight (kg)
EMAX 2306-2400kV	5x5x3	0.039
Sunnysky 2212-980kV	10x5x2	0.063
BrotherHobby 4215-520kV	13x12x3	0.217
Sunnysky X3520-8-520kV	12x6x2	0.232
HobbyPower T2204-2300kV	5x4x3	0.034
Elite 30cc	19x8x2	0.687
Sunnysky 3506-650kV	12x6x2	0.104
Gartt ML 4108-500kV	12x3.8x2	0.039
Tmotor U5-400kV	16x5.4x2	0.195
Tmotor U7-420kV	18x6.1x2	0.318
Tmotor MN605-170kV	20x6x2	0.327
Tmotor MN601-170kV	20x6x2	0.250

Data collected during this experiment was conducted rigorously by following several steps. The first step is to calibrate the thrust stand. There is a step-by-step procedure that is shown through the RC Benchmark software that is used to operate the thrust stand and calibrate the setup. This must be completed every time that the thrust stand is used to ensure good data acquisition. For this test stand specifically, the propeller must be installed in the pusher configuration to reduce the ground effects with the motor mounting plate [53]. Lastly, confirm that all safety measures are in place.

The motor-ESC efficiency was found by running each motor and propeller combination through a step-up in throttle test. A step-up throttle test starts from rest and increases the pulse width modulation (PWM) by small steps until the upper limit is reached. PWM is sent to the

ESC, which then drives the motor to produce torque to turn the propeller. Furthermore, each motor ran this test twice to ensure the accuracy of the results. With RPM, thrust, and electric power, motor-ESC efficiency can be calculated using

$$\eta_{\text{mot}}\eta_{\text{esc}} = \frac{P_{\text{mech}}}{P_{\text{elec}}} \tag{3.1}$$

where P_{elec} is the electric power measured by the thrust stand and P_{mech} is calculated using

$$P_{\text{mech}} = \Omega\tau \tag{3.2}$$

where τ is the torque and Ω is the rotational speed in radians per second. It is possible to get separate efficiencies for the motor and ESC, but for this thesis, it was not required so Equation 3.1 is used.

3.2 Vehicles

Three transitional vehicles of varying configurations were fabricated and tested to ensure a range of vehicles for consideration of weight models and vehicle performance predictions. All three vehicles were shown to be capable of maintaining a hover condition, forward flight condition, and transition between the two. These three vehicles, T1Ppy, Flippy, and Bronco, are shown in Figures 3.2, 3.3, and 3.4, respectively, and are described in terms of fabrication approach in Section 3.2.1, flight characteristics in Section 3.2.2, and dimensions and weight of vehicles in Section 3.2.3.

T1Ppy is a commercially available conventional fixed-wing vehicle (HEE Wing T-1 Ranger [54]) that was modified to perform as a bi-motor tail sitter. *Flippy* is a commercially available tri-motor thrust vectoring belly sitter (Jumper Xiake 800 [55]). The aft motor is stationary while the two wing-mounted motors are vectoring. *Bronco* is a commercially available bi-motor belly sitter (FliteTest FT Bronco [56]) that was converted into a 2-prop thrust vectoring vehicle with the use of custom 3D printed parts. T1Ppy uses differential thrust and control surfaces for control, while Flippy and Bronco are controlled with differential thrust, thrust vectoring, and control surfaces.

3.2.1 Fabrication

All these vehicles were modified from commercially available systems. In addition to the construction of the base vehicles, fabrication included a combination of electronic hardware

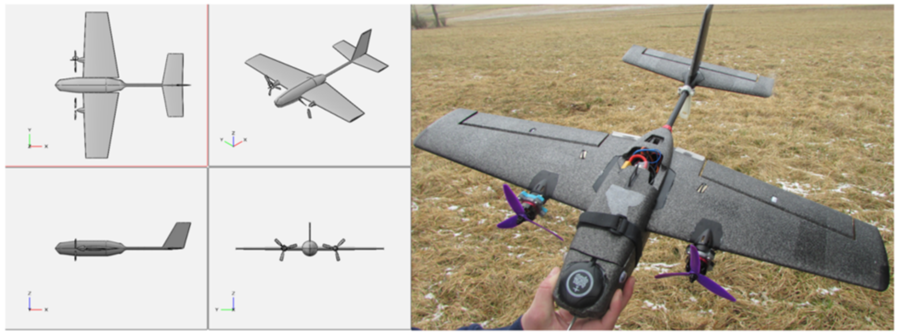

Figure 3.2: T1Ppy modeled to scale with 4 views (left) and picture of T1Ppy before flight testing (right).

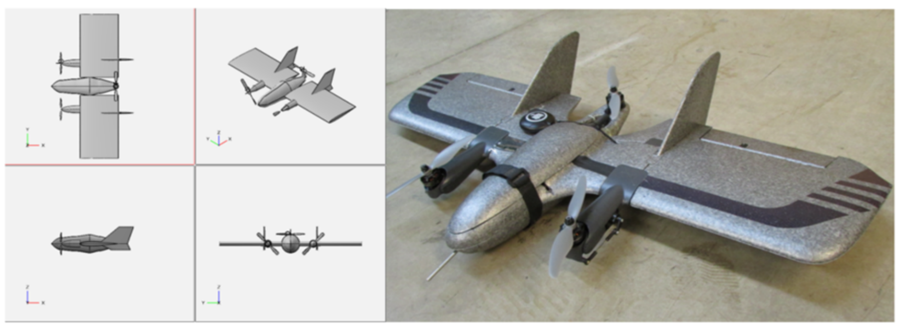

Figure 3.3: Flippy modeled to scale with 4 views (left) and a picture of Flippy before flight testing (right).

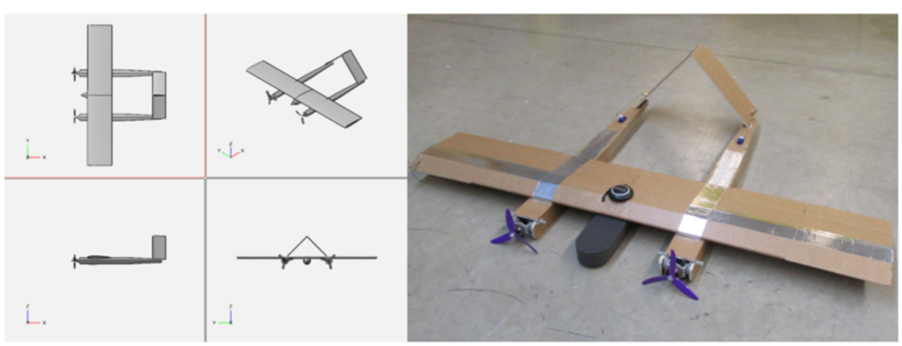

Figure 3.4: Bronco modeled to scale with 4 views (left) and a picture of Bronco before flight testing (right).

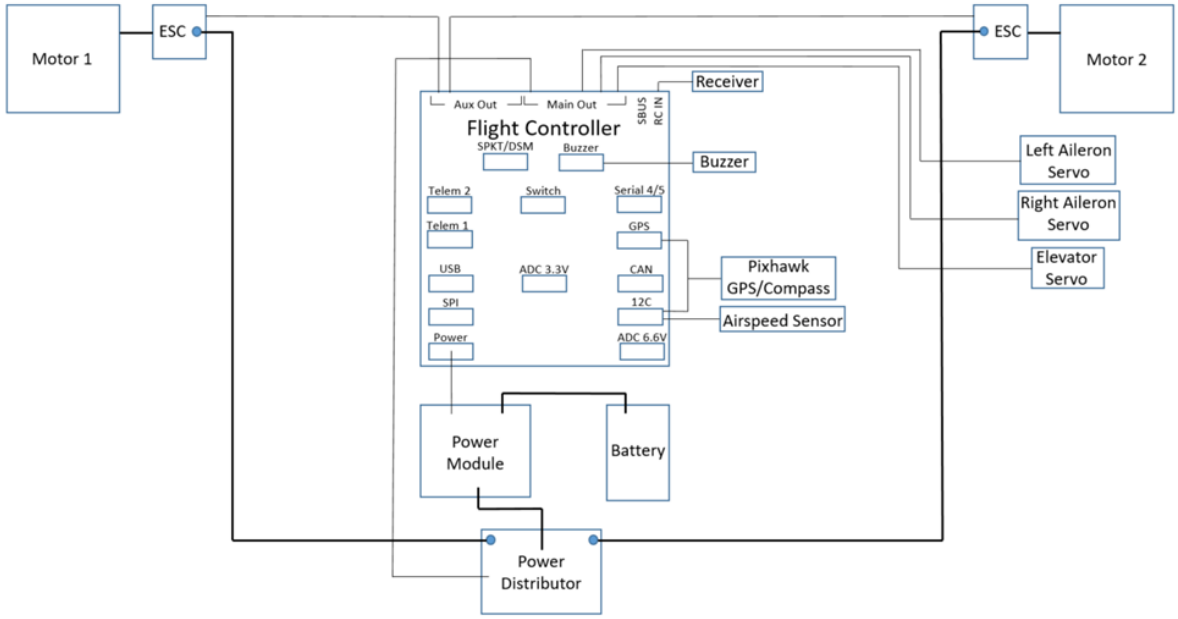

Figure 3.5: System/electrical diagram for T1Ppy.

replacement and integration, configuration of a flight controller, and additive manufacturing of custom parts. Because T1Ppy and Bronco were originally conventional fixed-wing aircraft, the recommended COTS motors and ESC were insufficient for VTOL capabilities. With this in mind, motors were selected based on a 1.5 thrust-to-weight ratio [23]. From there, the propeller was selected based on the motor manufacturer's provided combination. An ESC was selected based on the expected maximum current of the motor. For example, the motor, propeller, and ESC selected for Bronco was an EMAX ECOII2306-2400kV, HQProp 5x5x3, and Lumenier 51A BLHeli 32bit. Finally, additive manufactured parts were designed, printed, and integrated into the vehicle to enable VTOL capabilities.

An example of the electrical components that were used for the fabrication of these vehicles can be seen in the system/electrical diagram in Figure 3.5. The flight controller commands sub-systems and records data that is being received from internal and external sensors. The ESC controls the motors and the signal to the ESC comes from the flight controller. The actuators, which are connected to the flight controller, are used to command the control surfaces of the aircraft. Figure 3.5 is an example of T1Ppy's system and electrical diagram, however, Flippy's and Bronco's are similar.

In addition to the electronic components, 3D-printed parts were designed, printed, and integrated into the vehicle to allow for the VTOL capabilities to be achieved. To start, Flippy did not need any additional parts fabricated because the vehicle's base configuration already had

VTOL capabilities. T1Ppy used 3D-printed parts for a motor connection to the vehicle and for structural parts to have the ability to stand as a tail sitter. The motor connection was designed because different motors were selected than what the COTS part recommended. The tail-sitter structure parts were designed and integrated so T1Ppy would have the VTOL capability. Lastly, Bronco used 3D-printed parts for the thrust vectoring mechanism, which gave the vehicle VTOL capabilities. Bronco also used a custom 3D-printed electronic housing part.

After the physical fabrication of the three vehicles, the last step was to configure the flight controller, pilot's controller, and autopilot. This was primarily done in Mission Planner using Ardupilot firmware. Ardupilot is an open-source, trustworthy autopilot that has documentation for many different aircraft configurations [57].

3.2.2 Flight Characteristics

The flight characteristics of the three vehicles, as demonstrated through flight testing, are relevant because they give context to the results in Chapter 4, provide proof of flight, and give more information about the controllability of each configuration for vehicle design. The flight characteristics give an idea of how different configurations perform hover, transition, and forward flight. Proof of flight gives more context to how the vehicles performed in hover and forward flight in comparison to the results described in Chapter 4.

The proof of flight of T1Ppy transitioning from forward flight to hover is relevant to giving context to the performance results in hover and the controllability of tail sitters in hover. The progression of T1Ppy transitioning to hover from forward flight is shown in Figure 3.6. In forward flight, T1Ppy controls similarly to a conventional fixed-wing aircraft where thrust is provided by the motors, pitch control is provided by an elevator, roll control is accommodated with the ailerons, and there is no yaw control. Snapshots four, five, and six in Figure 3.6 show T1Ppy maintaining hover, however, snapshots sevens show the vehicle losing control in hover. T1Ppy was only able to maintain a hover for roughly a maximum 30 seconds during which there were frequent oscillations in propeller power and vehicle orientation. In hover, the aircraft's orientation changes relative to the ground where the roll control is provided by differential thrust, the pitch control is supplied by the now elevons and partially the elevator, and the yaw control is accommodated by the elevons. It is assumed that T1Ppy fails in hover because the pitch control is inadequate from the lack of control area from the elevons and elevator.

The proof of flights of Flippy taking off vertically and hovering, shown in Figure 3.7, and transition from hover to forward flight, shown in Figure 3.8, gives context to the forward flight and hover performance, along with the controllability of tricopters. Flippy is controllable and stable in takeoff and hover as shown in Figure 3.7. In hover, the roll control and pitch control

Figure 3.6: T1Ppy forward flight to hover transition.

Figure 3.7: Flippy vertical takeoff progression.

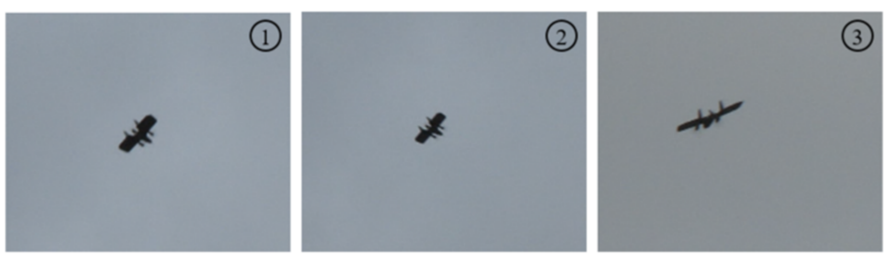

Figure 3.8: Flippy hover to forward flight transition progression.

are provided by differential thrust between the three propellers and yaw control is supplied by thrust vectoring of the front two motors. Flippy transition to forward flight is also controllable and stable, which provides context for tricopter's controllability across all flight domains. In forward flight, Flippy is a flying wing which means the thrust is provided by the two front motors, the roll and pitch axis is supplied by the elevons, and the yaw axis is provided by differential thrust between the two motors.

The proof of flights of Bronco taking off vertically, shown in Figure 3.9, and transitioning from hover to forward flight, shown in Figure 3.10, gives context to flight performance and controllability of 2-prop thrust vectoring vehicles. Bronco demonstrated that it is controllable

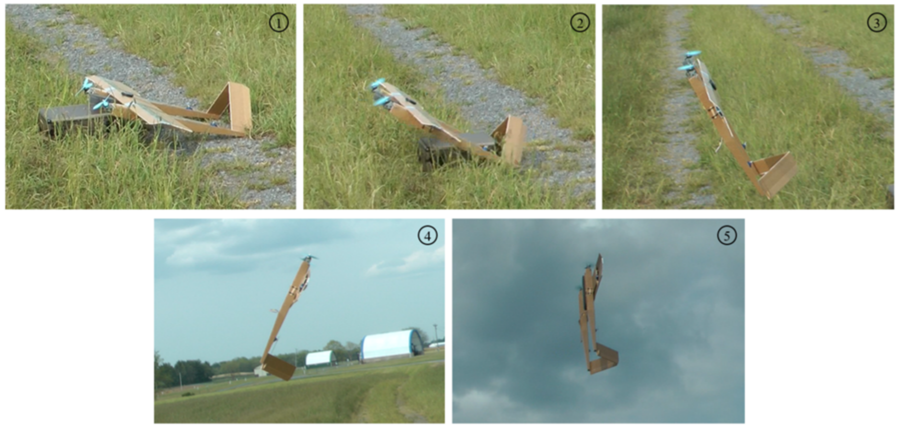

Figure 3.9: Bronco vertical takeoff progression.

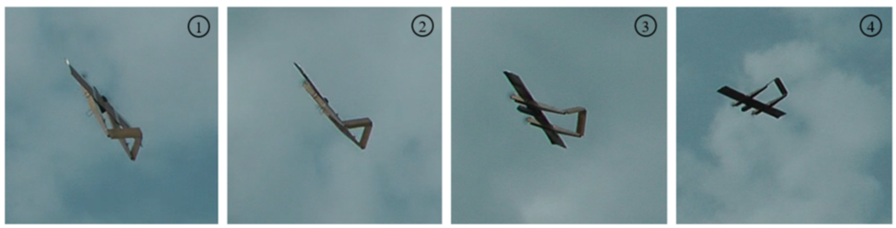

Figure 3.10: Bronco hover to forward flight transition progression.

and stable in vertical takeoff and hover as shown in Figure 3.9. In hover, Bronco's control is the same as T1Ppy except pitch control is provided by thrust vectoring. The downfall for non-thrust vectoring tail-sitters is the inability to successfully control the pitch in hover as thrust vectoring vehicles can. Bronco's transition from hover to forward flight is controllable and stable, which will provide context for the two-propeller thrust vectoring vehicle's controllability. In forward flight, Bronco is controlled similarly to T1Ppy as a conventional fixed-wing aircraft.

3.2.3 Dimensions and Weight

The vehicle dimensions and weight for T1Ppy, Flippy, and Bronco are shown in Table 3.2 and Table 3.3, respectively, which provides details into the scale of the vehicles and the results in Chapter 4. To clarify, Flippy has zero horizontal stabilizer area because it is a flying wing. When comparing the weights and vehicle dimensions of the three vehicles, certain trends appear, which should be understood before exploring the results. One of the major observations is that Bronco is the heaviest, with Flippy and T1Ppy being of similar weight. Bronco is the heaviest because of the structure of the vehicle. This can be seen with a larger wing area, longer fuselage, and larger overall tail area. Even though T1Ppy and Flippy have similar weights and sizes, the

Table 3.2: T1Ppy, Flippy, and Bronco vehicle dimensions.

	T1Ppy	Flippy	Bronco
Fuselage Length (in)	13.5	10.5	22
Fuselage Radius (in)	1.5	1.75	1.25
Propeller Solidity	0.21	0.1	0.23
Propeller Radius (in)	2.24	3	2.37
Number of Propellers	2	3	2
Number of Blades	3	2	3
Wing Area (in^2)	146	217	321
Wing Span (in)	26	28	43
Mean Chord (in)	5.6	7.8	7.5
Aspect Ratio	4.6	3.6	5.7
Taper Ratio	0.6	0.9	1
Vertical Stabilizer Area (in^2)	15.2	17.22	40
Horizontal Stabilizer Area (in^2)	43.8	0	40

Table 3.3: T1Ppy, Flippy, and Bronco weight breakdown in pounds (lbs).

	T1Ppy	Flippy	Bronco
Propellers	0.029	0.027	0.016
Motors	0.215	0.223	0.172
ESC's	0.117	0.097	0.226
Fuselage, Wing, Tail	0.643	0.701	1.131
Electronics/Avionics	0.342	0.343	0.342
Battery	0.424	0.424	0.424
Total w/o Battery	1.345	1.391	1.886
Total	1.769	1.815	2.365

propulsion systems of the two vehicles are different. This is seen with the difference in the number of propellers/motors, which can be denoted by differing numbers of blades, solidity, and radius.

3.3 Flight Testing

Flight testing is important to this thesis because it allows for data comparison to the design model proposed in Chapter 2. With accurate and repeatable flight test data, comparison and validation can be completed, as discussed in Chapter 4.

Several steps were taken to get accurate and repeatable flight test data for the three vehicles tested. Flight testing only occurred on fair weathered days, which generally meant under 5 mph

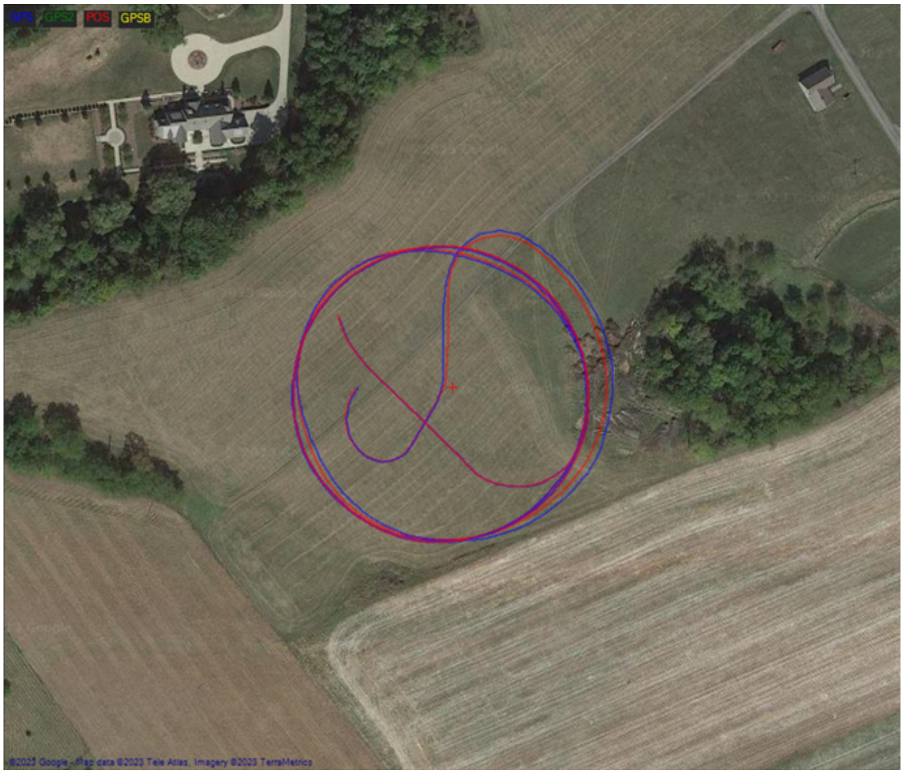

Figure 3.11: View of the flight path of the vehicle in forward flight for data recording, which is shown through Mission Planner.

winds with the occasional 10 mph winds maximum. Each vehicle underwent multiple flight tests that included both hovers and forward flights.

A hover, for this thesis, is defined to be when a vehicle stays in one place in the air for an extended period. Specifically for data recording, a hover would end when the vehicle exited a 5 ft error bound in altitude. This kept the data consistent and required the vehicle to be in stable hover. All vehicles completed two or more hover flights where the average and standard deviation were calculated for the power to hover. The recording method and flight controller are explained in Section 3.3.1.

Forward flight test for data collection was considered when the vehicle is flying in the pre-defined circle path at a specified airspeed. The assumption is that the flight path circle is large enough that the difference between flying straight and the circle is negligible. The circle radius was 60 meters and the vehicle completed a minimum of 3 loops around the circle before a forward flight test data would be considered complete. A typical flight path can be seen in Figure 3.11, and was completed using the autopilot.

3.3.1 Onboard Data Collection and Post Processing

The collection of data and post-processing is critical in understanding the results from flight testing in Chapter 4. The method of collecting and processing data for flight testing includes the pre-flight tasks, equipment on board the vehicle, and the procedure for examining the data.

The pre-flight tasks that were completed included calibrating the vehicle before flight testing, which comprised of calibrating the Pixhawk accelerometer and gyroscope, GPS, and voltage and current sensor. Calibrating the Pixhawk and GPS is completed through Mission Planner and involves orienting the vehicle in symmetry with Mission Planner's requests. Calibrating the voltage and current sensor includes running the motors with the propellers attached to at least 50% throttle so that the sensor is aligned with the recorded power drawn. *(Calibrating the voltage and current sensor can be dangerous because the vehicle's propellers are running while it is being held stationary.)*

The sensor equipment onboard the three different vehicles are similar which allowed for consistent data used in Chapter 4. The flight controller was a Pixhawk, which had the extra capability of data collection. The Pixhawk was equipped with a 32-bit ARM Cortex M4 core with FPU, MPU6000 three-axis accelerometer and gyroscope, and a MEAS barometer [58]. Several other external sensors were used for data collection, which were connected to the Pixhawk for data recording. The first is an airspeed sensor, specifically an mRo I2C Airspeed Sensor JST-GH-MS4525DO. This sensor consisted of a pitot-static probe and a digital transducer. The second sensor was a Ready to Sky Ublox M8N GPS that recorded ground speed, altitude, and heading. Lastly, a Holybro PM02 V2.0 voltage and current sensor was used to measure the power draw coming from the battery to the propulsion and avionics.

The procedure for examining the flight test data includes downloading the flight logs from the Pixhawk. The logs can be examined through the Mission Planner GUI or the logs can be converted into MAT files. When post-processing the data, it is important to note that different sensors record data at varying frequencies and timestamps.

The data was post-processed using averaging and standard deviations to get vehicle performance metrics. Hover flight tests were averaged over the length of time the vehicle stayed within the hover bounds as mentioned in Section 3.3. The average and standard deviation for power draw and length of time are recorded for each hover completed by the vehicles. Forward flight tests were averaged over the minimum three loops, as shown in Figure 3.11, for each specified airspeeds. The average and standard deviation for power draw and the average and standard deviation of airspeed are recorded for each forward flight by the vehicles. The data post-processed and recorded are discussed in Chapter 4.

Chapter 4
Design Model Validation

The definition of *validation* according to the American Institute of Aeronautics and Astronautics (AIAA) [59] is

> *The process of determining the degree to which a model is an accurate representation of the real world from the perspective of the intended use of the model.*

In this thesis, the intended use of the model is to design VTOL sUAS to complete missions that consist of hover, cruise, and loiter segments and transitions between them.

Proof of accuracy is required for use in the design methodology in two areas: power required and vehicle weight. Transition was proven for each vehicle configuration tested with proof of flight tests, however, energy use in transition was not modeled or validated because it was observed to be small compared to hover and forward flight energy consumption. As such, power required validation focused on proving that the model is capable of accurate prediction of hover power and forward flight power. Vehicle weights were compared with prediction both on a sub-component basis and in the aggregate.

One shortcoming to the validation described in this chapter results from the fact that each vehicle had to be developed in-house (see Section 3.2.1). The result is a very small dataset of three vehicles with only one in each configuration category. Because of this small data set, the data collected from these vehicles had to be used both to downselect models and to ensure their accuracy. An ideal alternative would be to use separate data sets to select models and validate; however, the development of additional vehicles was not possible for this work due to time constraints.

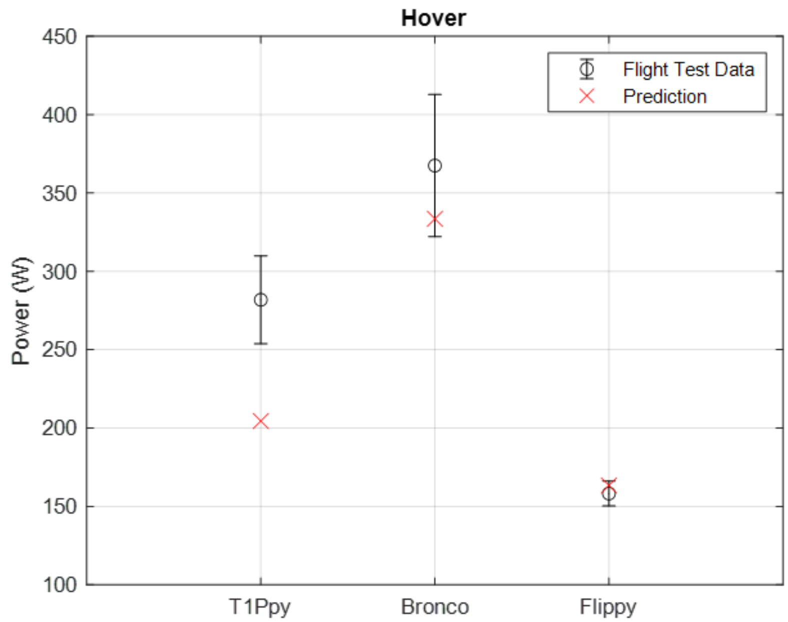

Figure 4.1: Power comparison between flight test data and design model for all vehicles.

4.1 Power Model Validation

4.1.1 Hover Validation

The predicted hover electrical power in comparison with the measured flight test data in hover is shown in Figure 4.1. The flight test data with error bars signify the average power consumption overall successful hover conditions plus and minus one standard deviation. Flippy's hover data has a small error bar spread because the hover condition was well stabilized, resulting in small changes in the power consumed and a larger data set to compute statistics. The average difference between the flight test mean and model prediction averaged for the three vehicles is 13.1%. Implementation of the correct motor speed and efficiency was critical in accurately modeling power for all three vehicles, as discussed further in Chapter 2. One potential source of the error between prediction and test data for T1Ppy is that it required significant autopilot control adjustments to maintain a hover.

4.1.2 Forward Flight Validation

Forward flight electrical power test data for T1Ppy, Bronco, and Flippy is provided in Figure 4.2 over a range of airspeeds. The three aircraft vary in wing area, weight, and configuration as

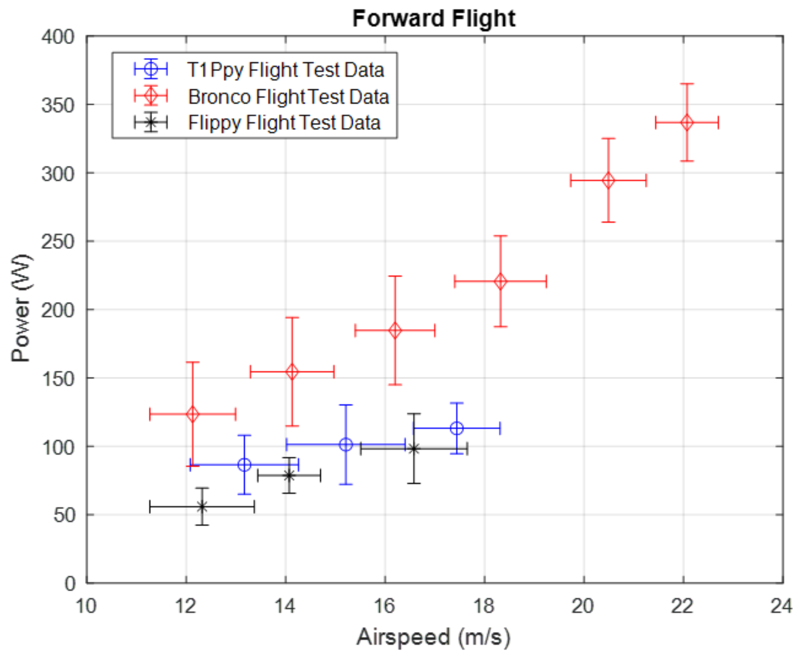

Figure 4.2: Electric power as a function of airspeed comparison of flight test data for T1Ppy, Bronco, Flippy.

previously mentioned in Section 3.2.3. Thus, the comparison of performance is not meaningful but provides context for differences between each vehicle tested.

A comparison of model predictions with flight test data for each of the vehicles is provided in Figures 4.3, 4.4, and 4.5. As discussed in Section 2.2.2, five models were considered for the fuselage drag. The design models shown include the same calculations for lifting surfaces with varying approaches to fuselage drag calculation. Hoerner's [44] and Babetto's [30] models are the most accurate for the flight test data as the power required is significantly under-predicted by the other three models. The average difference between the flight test mean averaged for the three vehicles is 20.1% and 57.5% for Hoerner's and Babetto's models, respectively.

It is evident from the flight test data that the method proposed by Hoerner is more accurate for the platforms analyzed in this thesis. The power required by T1Ppy is under-predicted across the velocity range. T1Ppy was also heavily modified from the stock version, likely resulting in trim drag and motor-ESC performance that was slightly off-design. The power required for Flippy and Bronco was well predicted across the velocity range.

To elucidate the influence of the fuselage model on the forward power predictions, it is helpful to explore an example breakdown of the drag using the Hoerner-based prediction as a function of airspeed. One such example is provided in Figure 4.6 for Flippy. Trends between the three aircraft were consistent. The fuselage drag was found to contribute the majority of the

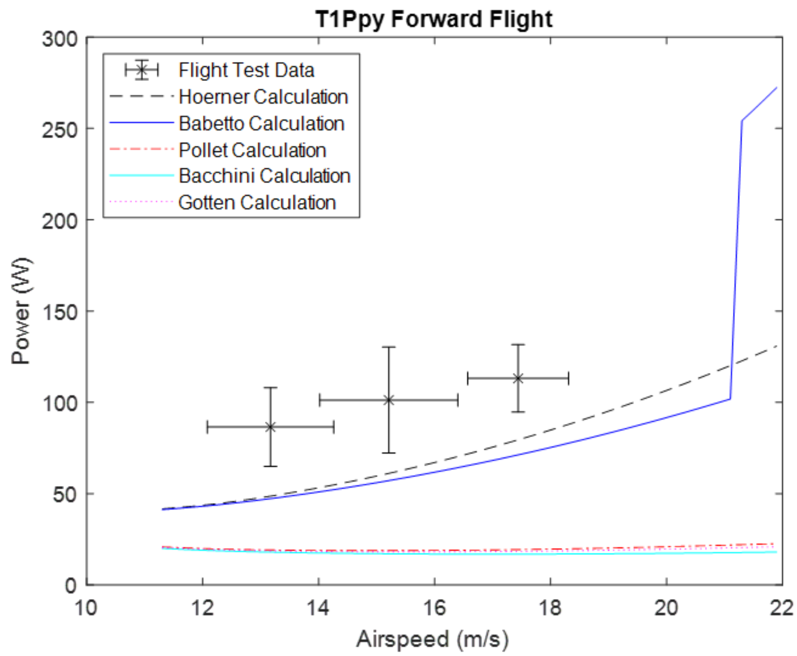

Figure 4.3: Electric power as a function of airspeed for forward flight data specifically for T1Ppy against different drag models.

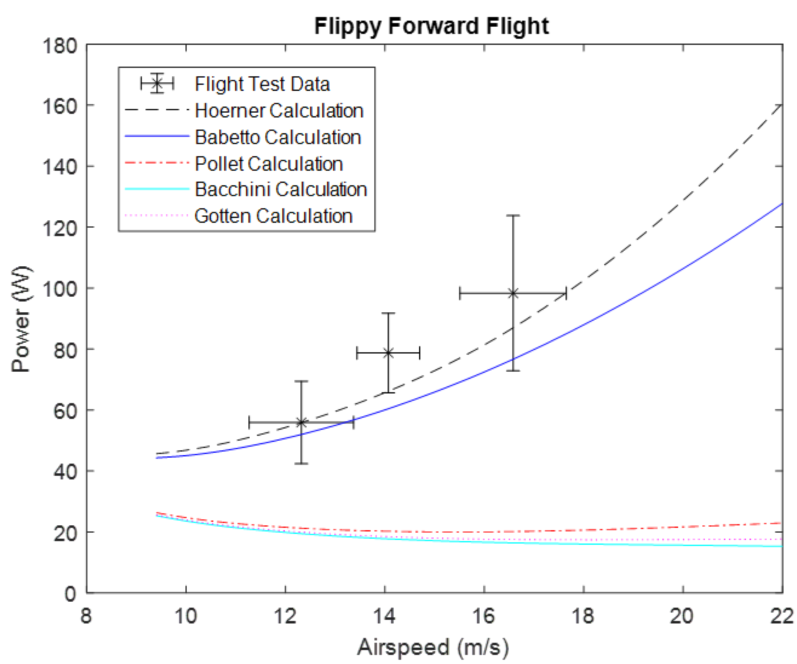

Figure 4.4: Electric power as a function of airspeed for forward flight data specifically for Flippy against different drag models.

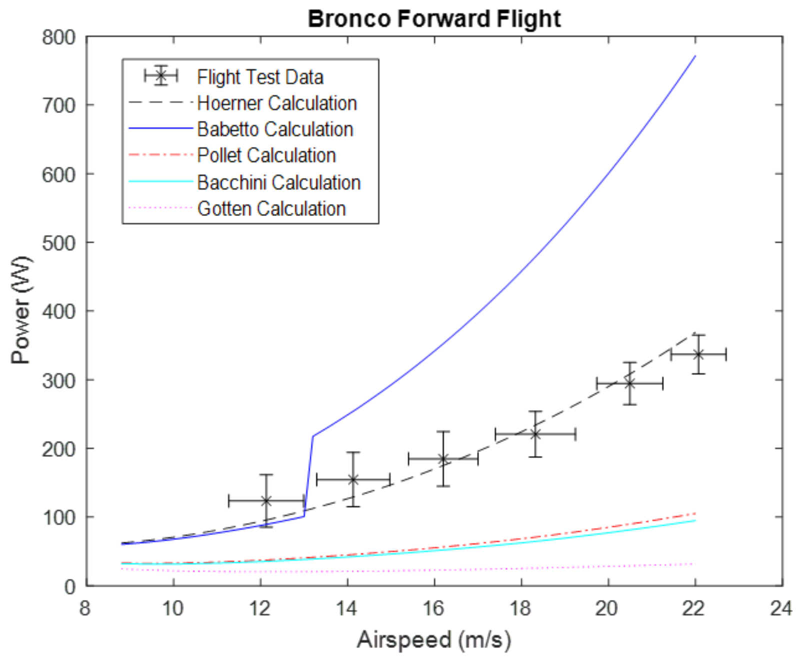

Figure 4.5: Electric power as a function of airspeed for forward flight data specifically for Bronco against different drag models.

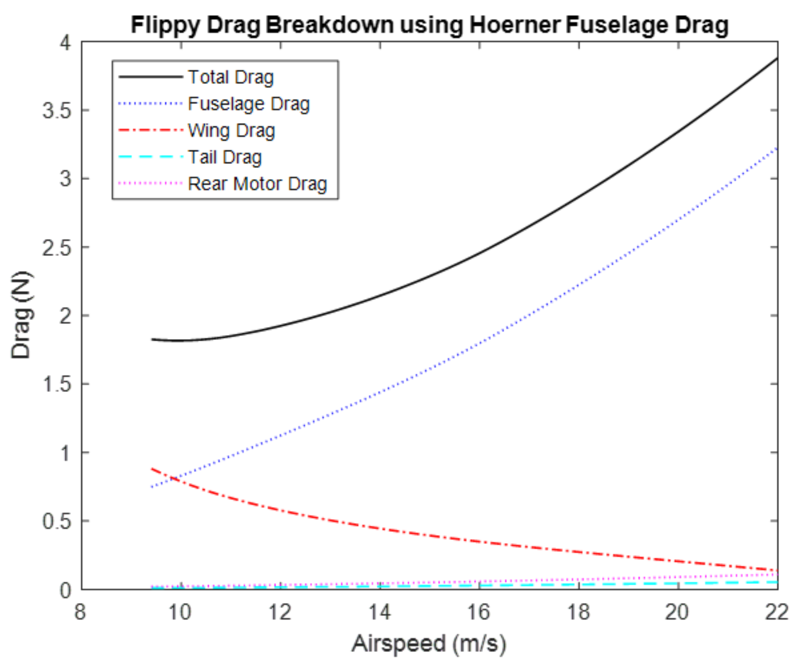

Figure 4.6: Drag as a function of airspeed for Flippy's breakdown of drag.

drag for this scale of vehicle over the flight speed range, while the third motor/propeller drag was found to be relatively negligible to the overall drag.

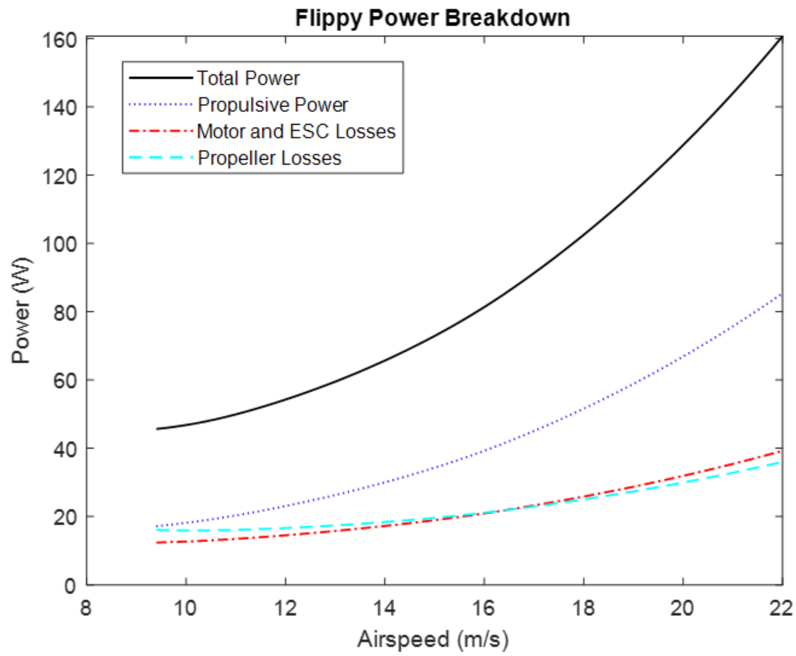

Figure 4.7: Power as a function of airspeed for Flippy's breakdown of power.

Another important factor in calculating the forward flight power accurately is having the correct motor, ESC, and propeller efficiencies. As mentioned in Section 2.1, the motor-ESC efficiency was estimated based on thrust stand testing and its effects can be seen in Figure 4.7. Similar to the hover calculations, the inefficiencies correlation for motor and ESCs at this scale is critical to accurately finding the power for forward flight. This is because the inefficiencies are a significant portion of the total power in forward flight.

4.2 Weight Model Validation

The last portion of the design model is the weight model. The weight model was created by collecting a set of equations for individual parts of the vehicles and testing them against the values found from T1Ppy, Flippy, and Bronco. Several equations predict sub-component weights as a fraction of the total vehicle weight and so the total vehicle weight of the as-flown configuration was used for these equations rather than the summation of the design model weights as provided in Chapter 2. In the design methodology, however, the dependence of the sub-component equations on the total weight of the vehicle indicates that the weight model would need to be iterative.

Table 4.1: Weight breakdown comparison between T1Ppy and design model.

	Actual Weight (lbs)	Design Model Weight (lbs)	Difference (lbs)
Propellers	0.029	0.015	0.014
Motors	0.215	0.162	0.053
ESC's	0.117	0.044	0.073
Fuselage, Tail	0.346	0.253	0.093
Wing	0.297	0.222	0.075
Electronics/Avionics	0.342	0.296	0.046
Battery Weight	0.424	0.424	—
Total	1.769	1.415	0.354

The weight breakdown comparison between T1Ppy and the design weight model is provided in Table 4.1. The difference in total weight between T1Ppy and the design model is 20%. The weight breakdown comparison between Flippy and the design model is shown in Table 4.2. The difference in total weight between Flippy and the design model is 6.4%. The weight breakdown comparison between Bronco and the design model is provided in Table 4.3. The difference in total weight between Bronco and the design model is 0.2%. For this comparison, the battery weight was input, but for the design methodology, Equation 2.50 is used. Overall, the total average weight difference between the design model and the three vehicles is 8.7%.

It is important to note that there is a large variability weights at this scale due to the quality of the build and materials used in the construction of the motors. An example of this variability can be seen in the motors for T1Ppy and Bronco. The motors for T1Ppy were EMAX RS2205-2300kV and the motors for Bronco were EMAX ECOII2306-2400kV. The motors for Bronco can support more thrust than T1Ppy's motors, however T1Ppy's motors are heavier. The comparison between T1Ppy's and Bronco's motor weight and capability is not the same as the relation shown in Figure 2.1. Currently, there is no method to model the differences between manufacturer design and fabrication choices.

Table 4.2: Weight breakdown comparison between Flippy and design model.

	Actual Weight (lbs)	Design Model Weight (lbs)	Difference (lbs)
Propellers	0.027	0.023	0.004
Motors	0.223	0.155	0.068
ESC's	0.097	0.042	0.055
Fuselage, Tail, Wing, Transition Mechanism	0.701	0.747	−0.046
Electronics/Avionics	0.343	0.307	0.035
Battery Weight	0.424	0.424	—
Total	1.815	1.698	0.117

Table 4.3: Weight breakdown comparison between Bronco and design model.

	Actual Weight (lbs)	Design Model Weight (lbs)	Difference (lbs)
Propellers	0.016	0.016	0.000
Motors	0.172	0.248	−0.076
ESC's	0.226	0.072	0.154
Transition Mechanism	0.146	0.116	0.030
Fuselage + Tail	0.447	0.418	0.029
Wing	0.538	0.649	−0.111
Electronics/Avionics	0.342	0.428	−0.085
Battery Weight	0.424	0.424	—
Total	2.365	2.370	−0.005

Chapter 5 | Design Methodology

This chapter presents the design methodology developed for the conceptual design of VTOL sUAS as described in the flow chart shown in Figure 5.1. The design methodology is based on a previous design methodology for the conceptual design of full-scale electric helicopters [29]. Two iterative processes are used to design the vehicle: the aero-propulsive design and the integrated vehicle design. The aero-propulsive design is completed using estimates and iterated on until it meets the design constraints as described in Section 5.2. The second iterative process focuses on ensuring the vehicle can complete the mission based on the predicted power required and battery size, as described in Section 5.3. Once both processes are complete, a conceptually designed VTOL sUAS is found.

5.1 Initialization and Constraints

The start of the design process is driven by the initial inputs for the vehicle, as shown in Figure 5.1. The major inputs into the design methodology are the mission profile, payload weight, and configuration type. Available mission segments include vertical takeoff/landing, hover, climb/descent, transition, loiter, and cruise. The configuration type selected dictates the component models required both in terms of power and weight.

The next step in the design methodology is the initial estimate of the vehicle's weight and inputs of other vehicle parameters based on the configuration selected. The initial estimate of the vehicle's weight (W_{tot} in lbs) is found using an empirical relation from Ref. [3] for unmanned VTOL vehicles between 2 and 150 pounds using the relationship

$$W_{\text{tot}} = \frac{W_{\text{pay}} - 0.004}{0.244} \tag{5.1}$$

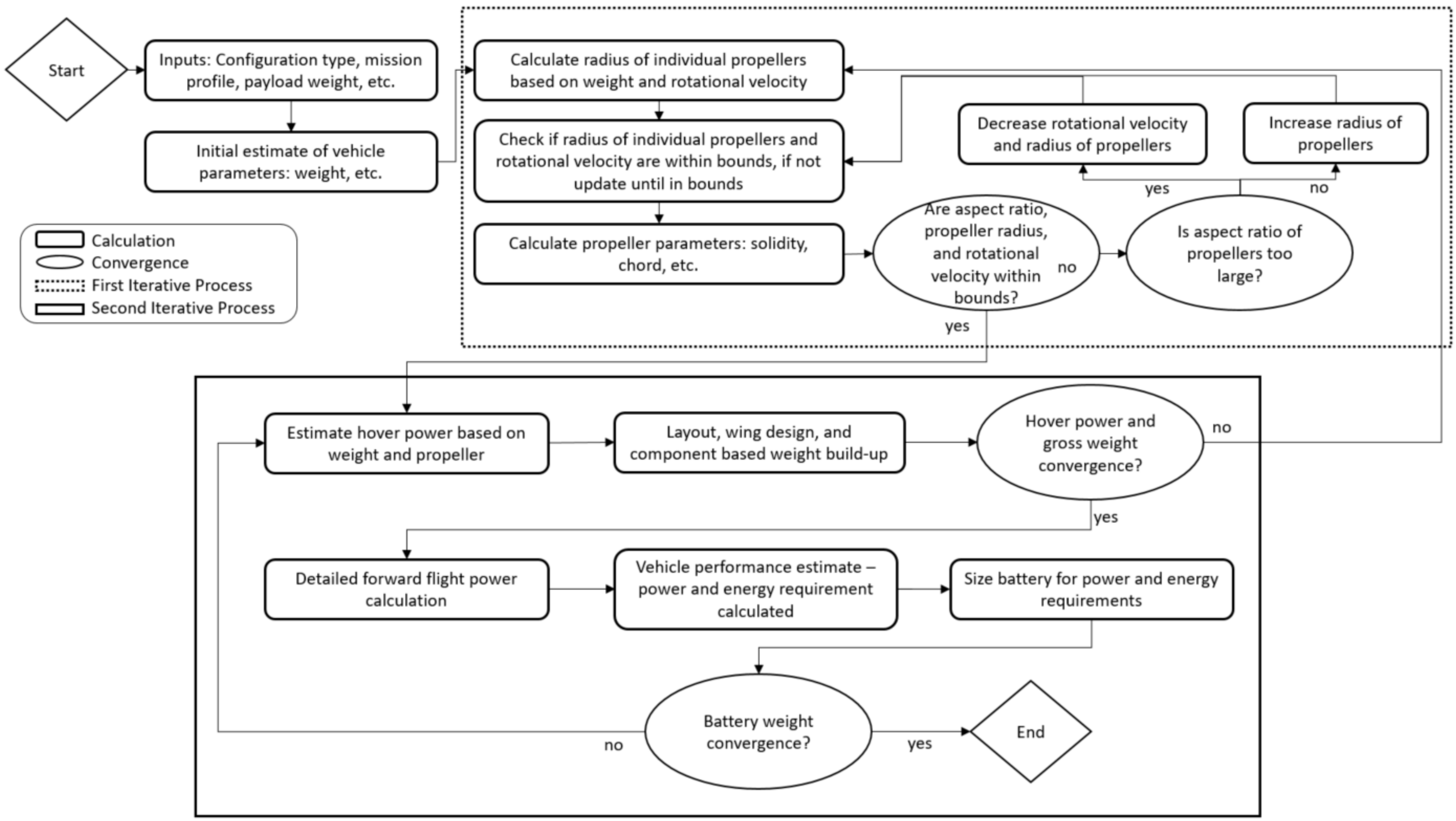

Figure 5.1: Flowchart of the design methodology.

Table 5.1: Constraints used within the design methodology.

Parameter	Assumption	Justification
Maximum Rotational Velocity (rad/s)	Calculated maximum rotational velocity	Mach Effects [41]
Minimum Rotational Velocity (rad/s)	20	n/a
Maximum Propeller Radius (m)	0.51	[60]
Minimum Propeller Radius (m)	0.02	[61]
Maximum Aspect Ratio	20	[62]
Minimum Aspect Ratio	5	Section 3.2.3

where W_{pay} is the weight of the payload in lbs, which was an initial guess into the design methodology. The other initialized vehicle parameters are the number of rotors, the number of blades, disk loading, airspeed, fineness ratio, fuselage radius, aspect and taper ratio, and wing thickness. These parameters were either selected based on the configuration selected or by a sensitivity analysis, which is explained in further detail in Section 6.1.

There are many assumed constraints for the design methodology, which are shown in Table 5.1. The maximum rotational velocity comes from the tip speed of the propeller not exceeding 65% of the speed of sound. The minimum and maximum of the propeller radius for VTOL sUAS are 0.02 and 0.51 meters, respectively, from the largest and smallest fixed-pitch propeller sold commercially for VTOL sUAS [60, 61]. The maximum rotational velocity is calculated in Section 5.2 and the minimum is set to 20 rad/s, however, the minimum rotational velocity is not a limiting factor. The maximum aspect ratio for the propeller is 20 based on Kee [62] and the minimum aspect ratio is based on previous experience discussed in Section 3.2.3.

5.2 Propulsion Design

The first step in the propulsion design process is calculating the radius based on the weight and initializing the rotational velocity. The rotational velocity of the propeller is initialized as half of the maximum rotational velocity (see Table 5.1). The half multiplier is based on experience from the RPMs derived from both flight testing and thrust stand testing in Section 3.2.2 and 3.1, respectively. The radius of an individual propeller is calculated by

$$R_{\text{rotor}} = \sqrt{\frac{A_{\text{rotor}}}{\pi}} \tag{5.2}$$

where A_{rotor} is calculated from Leishman [41] as

$$A_{\text{rotor}} = \frac{T_{\text{rotor}}}{DL} \tag{5.3}$$

where DL is the disk loading and T_{rotor}, in this case, is the initial estimate of vehicle weight divided by the number of propellers.

The next step is checking if the radius and rotational velocity of the propeller are within the bounds set. If the radius is too large, the radius is decreased until it is within the bounds and vice versa. If the rotational velocity is above the upper bound, the rotational velocity is decreased until it is within the bounds and vice versa.

The last calculation step in the propulsion design iterative process is calculating the propeller parameters, which are solidity, chord, and aspect ratio. The solidity is calculated from [41] as

$$\sigma = \frac{C_T}{BL} \tag{5.4}$$

where BL is the blade loading, which is the gross weight of the vehicle divided by the total area of the propeller blades. A correlation between the advance ratio and blade loading from Kee [62] was used to estimate the blade loading. With this correlation, the blade loading coefficient is determined by using linear interpolation. C_T is the thrust coefficient of an individual propeller, which is found with

$$C_T = \frac{W_{\text{tot}}}{n_{\text{rotor}} A_{\text{rotor}} \rho V_{\text{tip}}^2} \tag{5.5}$$

where V_{tip} is the tip speed velocity of the propeller and calculated as

$$V_{\text{tip}} = \Omega R_{\text{rotor}}. \tag{5.6}$$

The last step in the first iterative process is comparing the resultant propeller to the design constraints. It is assumed for this portion of the design that the propellers are rectangular. Based on whether or not the aspect ratio is too large or too small, the radius is either decreased or increased while the rotational velocity is also changed. Once the propulsion system reaches the design constraints, the first iterative process is complete.

5.3 Integrated Vehicle Design

The second major iterative process is the integrated vehicle design. Many of the components in this second iterative process were introduced in detail in Chapter 2 and validated in Chapter 4.

The first of these steps is the estimation of hover power based on weight and the designed propeller. The hover power calculation was examined in Section 2.1 and validated in Section 4.1.1.

The next step in the design methodology is the layout and component-based weight build-up. The component weight build-up was examined in Section 2.3 and validated in Section 4.2. The layout of the components for the vehicles depends on the vehicle configuration. For example, vehicle configurations with a wing require sizing of the lifting surface. The wing area calculated from [63] as

$$S_{\text{wing}} = \frac{W_{\text{tot}}}{\frac{1}{2}\rho V_\infty^2 \sqrt{\pi Æ_{\text{wing}} e_{\text{wing}} c_{do}}} \tag{5.7}$$

where e_{wing} is the Oswald's efficiency factor of the wing and c_{do} is the zero-lift drag coefficient assumed from Raymer [63]. The span of the wing is found using

$$b = \sqrt{Æ_{\text{wing}} S_{\text{wing}}} \quad . \tag{5.8}$$

The average wing chord is found using

$$\bar{c} = \frac{S_{\text{wing}}}{b} \quad . \tag{5.9}$$

The root and tip chord can be found with the taper ratio, λ, using the following calculation

$$c_{\text{root}} = \frac{2\bar{c}}{1+\lambda} \tag{5.10}$$

$$c_{\text{tip}} = c_{\text{root}}\lambda \quad , \tag{5.11}$$

respectively. The spar length for the quadrotor arms is based on the rotor radius from the propulsion design. The spar length is the rotor radius multiplied by 1.75, which is calculated based on leaving half of the propeller radius as the clearance between each of the four propellers.

After total vehicle weight build-up is complete and hover power is calculated, a convergence test for both is examined. The criterion requirement for convergence of both hover power and vehicle gross weight is 1%. If convergence is not found, the new weight is used to start the aero-propulsive design process over again, as shown in Figure 5.1.

With gross weight and hover convergence, the next step is to estimate the forward flight power. This changes based on the configuration selected, however, this step is explained in detail in Section 2.2 and validated in Section 4.1.2.

With the forward flight power and hover power estimated, the vehicle's performance is calculated based on the power and energy requirements. Using the estimated forward flight power and hover power results, the maximum power and energy capacity requirements can be acquired. The energy capacity is calculated based on the mission profile and the calculated hover power and forward flight power.

Once the vehicle's power and energy requirements are calculated, the battery for the vehicle can be sized. Based on the battery's chemical composition, the maximum power requirements or the energy capacity requirements could be the driving factor in the battery size. In addition, it is assumed that only 70% of the battery can be used during flight because of battery limitations and incorporating a reserve for emergency actions, which is typically recommended by the FAA [1]. For current COTS batteries, the battery limitations for safe discharge limits to preserve battery life is between 80-85% [64, 65]. The battery's specific energy and power density are given as inputs. For example based on currently commercially available battery options, a lithium polymer battery has a specific energy of 158 watt hours per kg and a power density of 430 watts per kg [50].

Lastly, battery convergence is checked. If the battery weight has converged, then the design process for VTOL sUAS is complete. However, if the battery weight did not converge, then the second iterative process in the design methodology is restarted using a new total weight based on the new battery weight.

Chapter 6
Mission Space Exploration and Vehicle Design

This chapter explores the mission space using the design methodology from Chapter 5 as a case study comparing a *quadrotor* and a *2-prop thrust vectoring vehicle* over a set of potential missions as shown in Section 6.1. Both vehicles are run through design studies against mission spaces defined by range and endurance goals to identify regions where one configuration is preferred over the other as shown in Section 6.1.2. Based on a mission determined from the mission space exploration, a 2-prop thrust vectoring vehicle is designed using the design methodology in Section 6.2.

6.1 Case Study Between 2-Prop Thrust Vectoring Vehicle and Quadrotor

A mission space exploration was completed to determine the bounds of the feasible mission space for a quadrotor and 2-prop thrust vectoring vehicle. Although the method is capable of designing several configurations (as discussed in previous chapters), the 2-prop thrust vectoring vehicle and quadrotor were chosen for comparison for several reasons. The first reason is because of the controllability of the vehicle in hover, forward flight, and transition as discussed in Section 3.2.2. Tail sitters were difficult to control in hover while tri-copters and 2-prop thrust vectoring vehicles were easier to control in all VTOL flight domains. When downselecting between a tri-copter and 2-prop thrust vectoring vehicle, the disadvantages, advantages, and component complexity were compared (see Section 1.1.2). The 2-prop thrust vectoring vehicle and tri-copter were tied with the least amount of disadvantages and the most amount of advantages, as shown in Table 1.1. The 2-prop thrust vectoring vehicle was finally downselected based on having fewer components than the tri-copter, as shown in Table 1.2. On the other hand, the quadrotor was selected as the configuration to compare against because of its popularity for VTOL sUAS, lack of wing as a lifting surface, and its controllability in hover and forward flight.

6.1.1 Sensitivity Analysis

Before running the mission space exploration, sensitivity tests were run to determine some initial parameters, as mentioned in Section 5.2. Sensitivity analysis for this thesis is varying multiple vehicle parameters and selecting parameter values based on the resultant trends. The baseline mission run for the sensitivity analysis was a 1 mile forward flight and 1 minute hover. This was selected as the mission for sensitivity analysis because the changes in total weight and total energy capacity were examined rather than the longest mission possible. Disk loading was assumed to be 2.0 $^{lbs}/_{ft^2}$. The parameters that underwent sensitivity tests were airspeed and fineness ratio for varying payloads. The sensitivity analysis was completed using the Applied Research Laboratory Trade Space Exploration (ATSV) tool [66].

The quadrotor sensitivity analysis for cruise speed and fineness ratio is shown in Figures 6.1 and 6.2, respectively. For the quadrotor, the gross weight was used as an indicator for which vehicle is the "best" design, as discussed in Section 1.1.1. With gross weight as the indicator, the quadrotor is optimal at a cruise speed of 7.5 m/s. This was selected as the cruise speed for the quadrotor for the mission space exploration. The trend of decreasing gross weight as the fineness ratio decreases is shown in Figure 6.2. This trend can be explained because, for a quadrotor, the fuselage is not as streamlined as it is for the 2-prop thrust vectoring vehicle, but rather a cylinder that houses the electronics. The smaller the cylinder in the cross-sectional flow in forward flight, the less power is required, which results in a smaller gross weight. A fineness ratio of 3 was selected to ensure enough room in the fuselage to incorporate all of the electronics necessary, even though it does not result in the lightest vehicle.

The sensitivity analysis for the 2-prop thrust vectoring vehicle for cruise speed and fineness ratio is shown in Figures 6.3 and 6.4, respectively. As discussed in Section 1.1.1, total energy capacity and gross weight can be indicators of the "best" vehicle design. For the 2-prop thrust vectoring vehicle sensitivity analysis, gross weight, and total energy capacity were balanced to decide vehicle parameters. For a 0.25 lbs payload, a cruise speed of 16 m/s and a fineness ratio of 3 was selected from Figures 6.3 and 6.4.

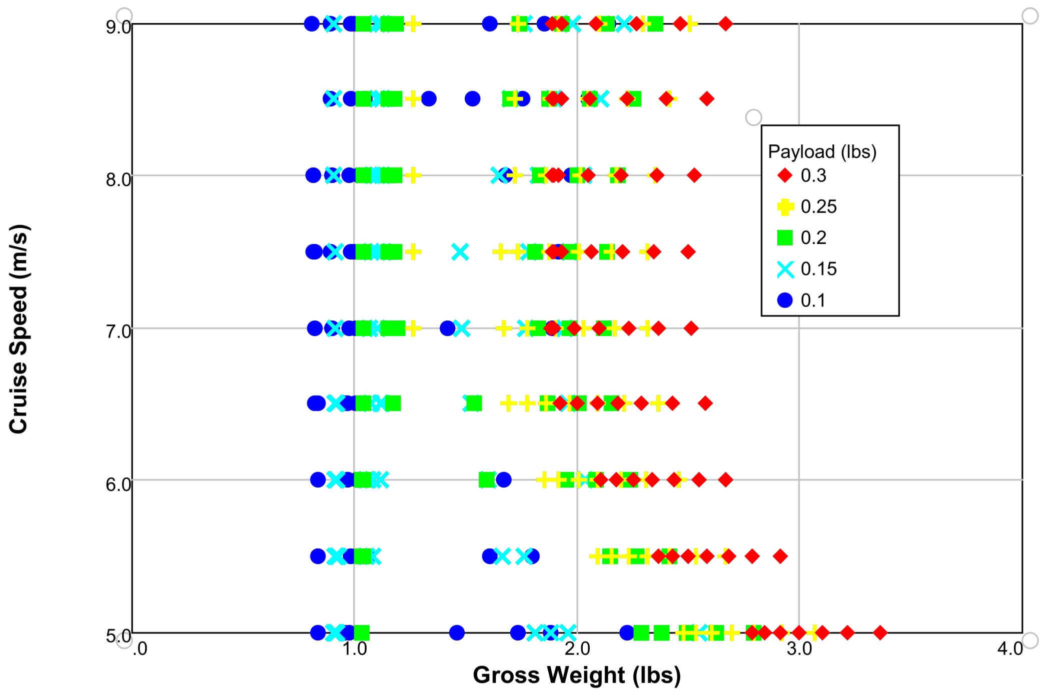

Figure 6.1: Cruise speed as a function of gross weight for quadrotor sensitivity test for varying payloads.

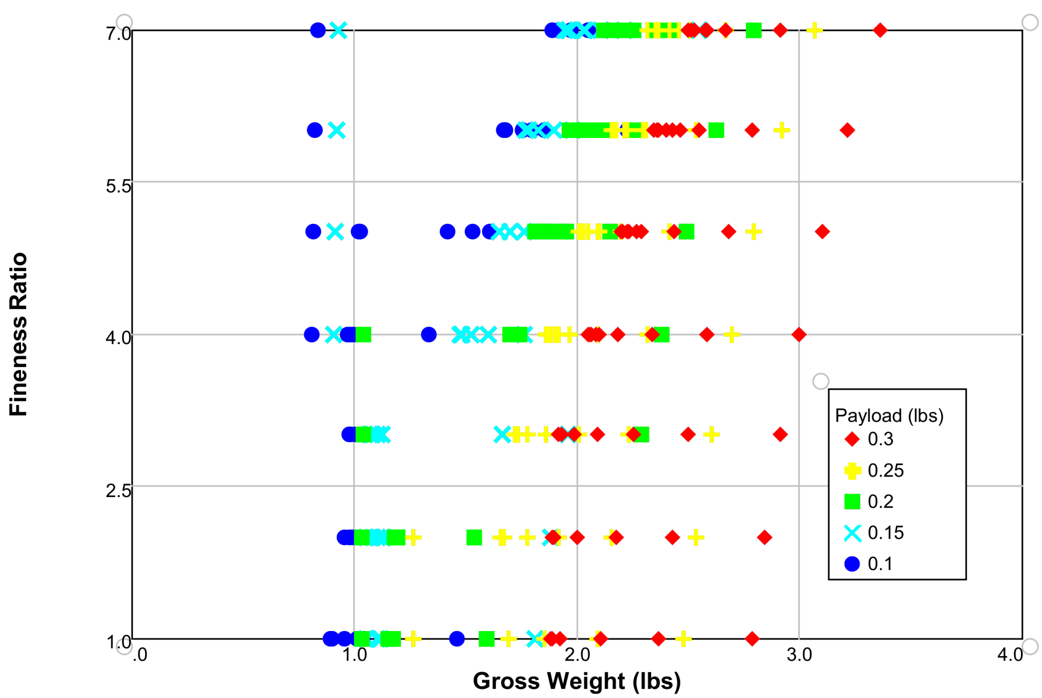

Figure 6.2: Fineness ratio as a function of gross weight for quadrotor sensitivity test for varying payloads.

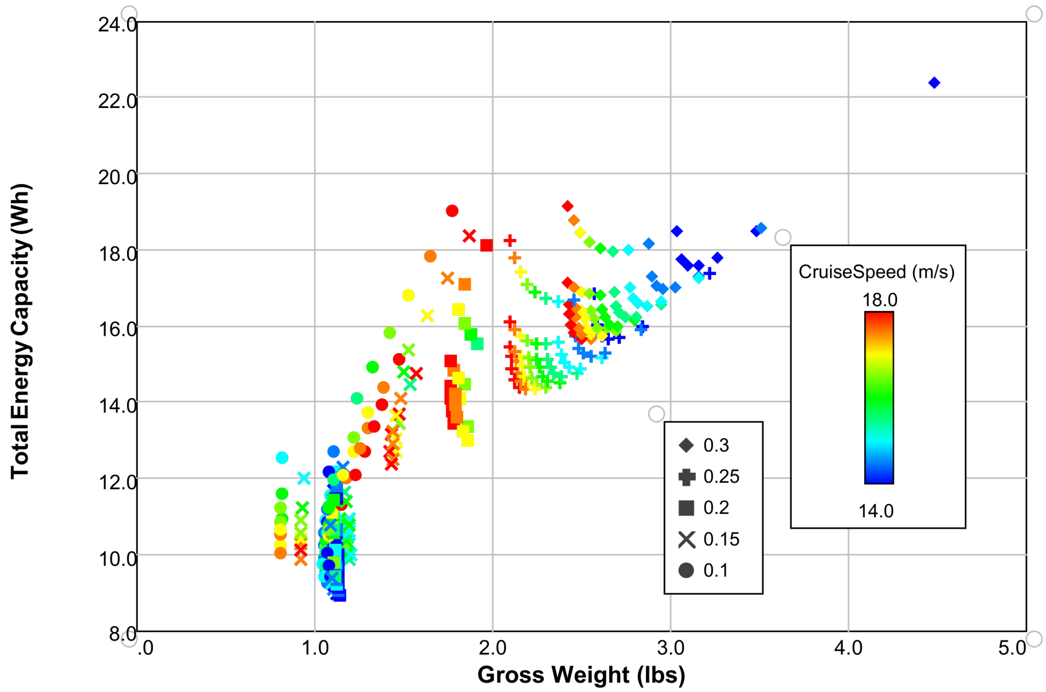

Figure 6.3: Sensitivity analysis for 2-prop thrust vectoring vehicle with gross weight against total energy capacity for varying airspeed denoted by color and varying payload denoted by markers.

6.1.2 Mission Space Exploration

With the tests complete for both the quadrotor and the 2-prop thrust vectoring vehicle, the mission space was explored for both sUAS vehicle configurations. Using the design methodology, the two vehicles were run for a range of missions, which varied hover time and forward flight distance. The two edge cases were whether the vehicle converged through the design methodology or if the vehicle was under 55 lbs per FAA regulations on sUAS. The resulting mission space exploration was run with a 0.25 lb payload.

The gross weight of the quadrotor and total energy capacity against varying missions of distances and hover times are shown in Figures 6.5 and 6.6, respectively. For cases of the quadrotor at 0.25 pounds payload, the limiting factor in the design was non-convergence rather than the 55 lbs maximum.

A similar mission space exploration was completed for the 2-prop thrust vectoring vehicle with a 0.25 lb payload. The gross weight of the 2-prop thrust vectoring vehicle and total energy capacity against varying missions of distances and hover times are shown in Figures 6.5 and 6.6, respectively. In Figure 6.7, there is a flat-lined gross weight where the gross weight does not increase as the mission increases, which is also seen with the quadrotor in Figure 6.5. This

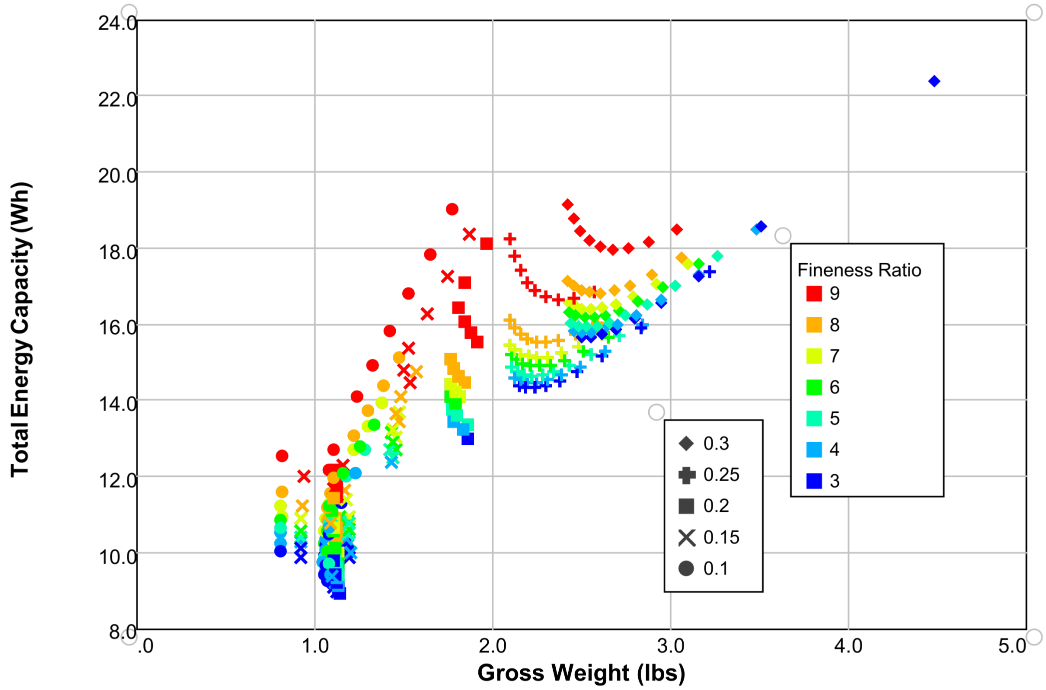

Figure 6.4: Sensitivity analysis for 2-prop thrust vectoring vehicle with gross weigh against total energy capacity for varying fineness denoted by color and varying payload denoted by markers.

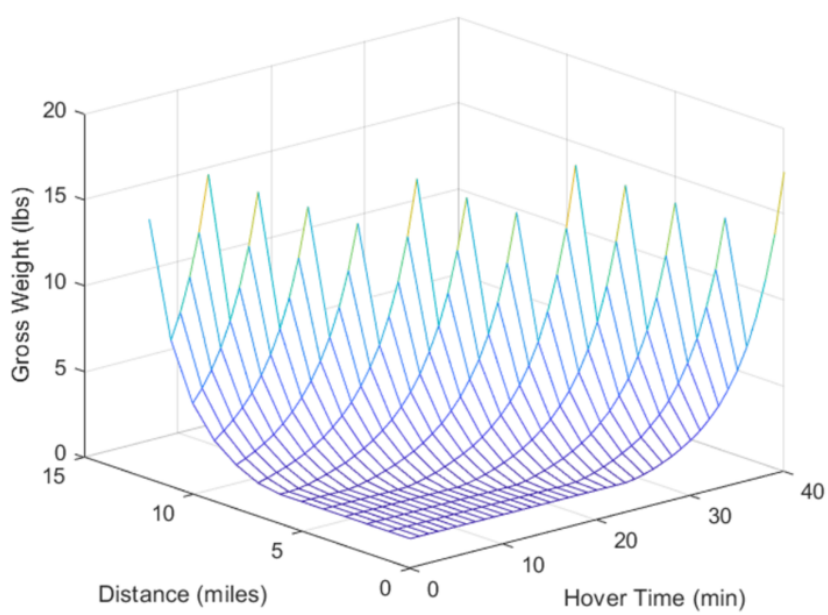

Figure 6.5: Gross weight based on a mission for quadrotor.

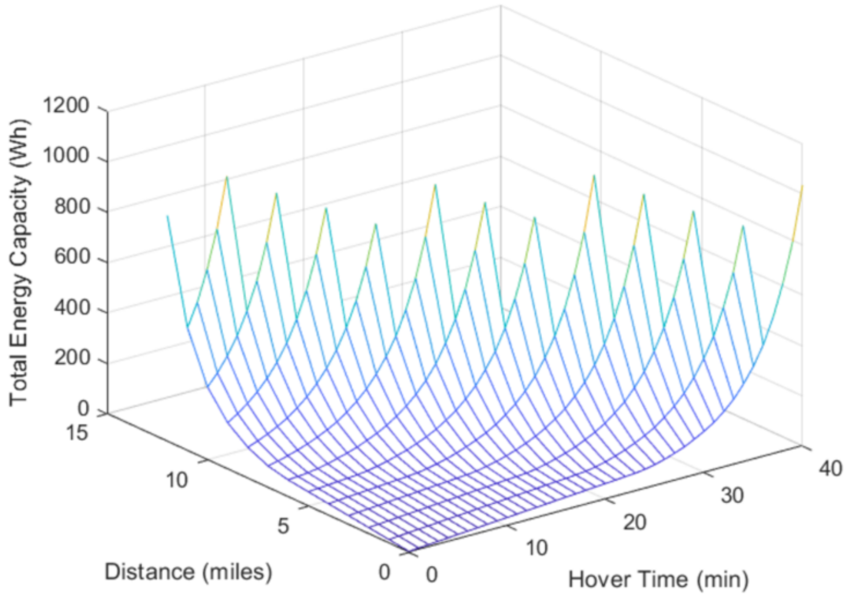

Figure 6.6: Total energy capacity based on a mission for quadrotor.

occurs because the battery is being sized based on the power draw needed for hover rather than the total energy capacity needed.

A comparison of the mission space of both the quadrotor and 2-prop thrust vectoring vehicles is shown in Figure 6.9. Each point in the space refers to an individual design of either a quadrotor or a 2-prop thrust vectoring vehicle. As expected, the quadrotor can complete long hover times while the 2-prop thrust vectoring vehicle cannot. In addition, the quadrotor cannot complete long distances compared to a vehicle with a lifting surface.

Based on design objectives described in Section 1.1.1, both vehicles were examined based on the lightest vehicle and most energy efficient for a given mission. The interesting portion is the crossover zone where both vehicles can operate. The lightest vehicle, in terms of gross weight, for the mission space is shown in Figure 6.10. The most energy-efficient vehicle, in terms of total energy capacity, for the mission space is shown in Figure 6.11. There are some cases where the lightest vehicle is not always the most energy efficient, which aligns with the original discussion of design objectives. Based on the requirements of the design, one could want the lightest vehicle or the most energy-efficient vehicle.

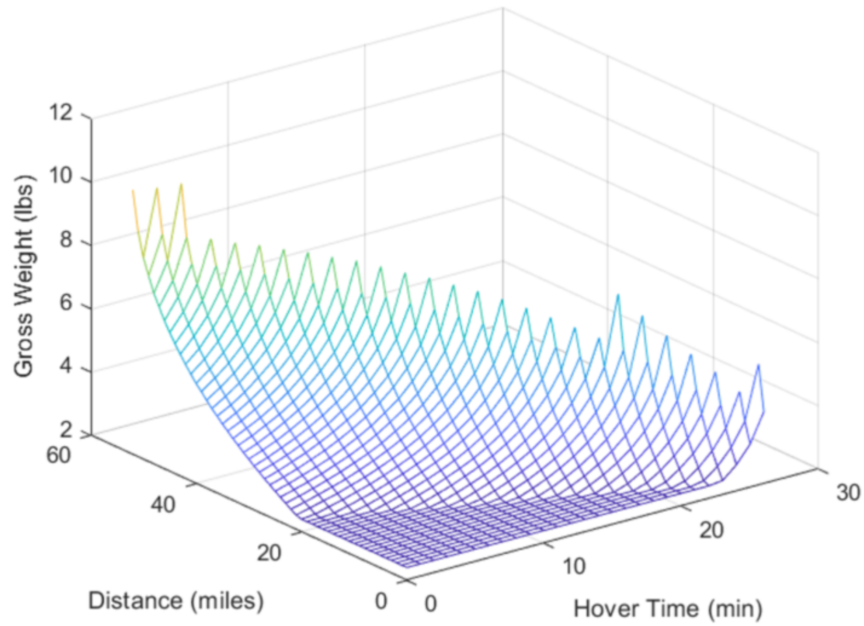

Figure 6.7: Gross weight based on mission for 2-prop thrust vectoring vehicle.

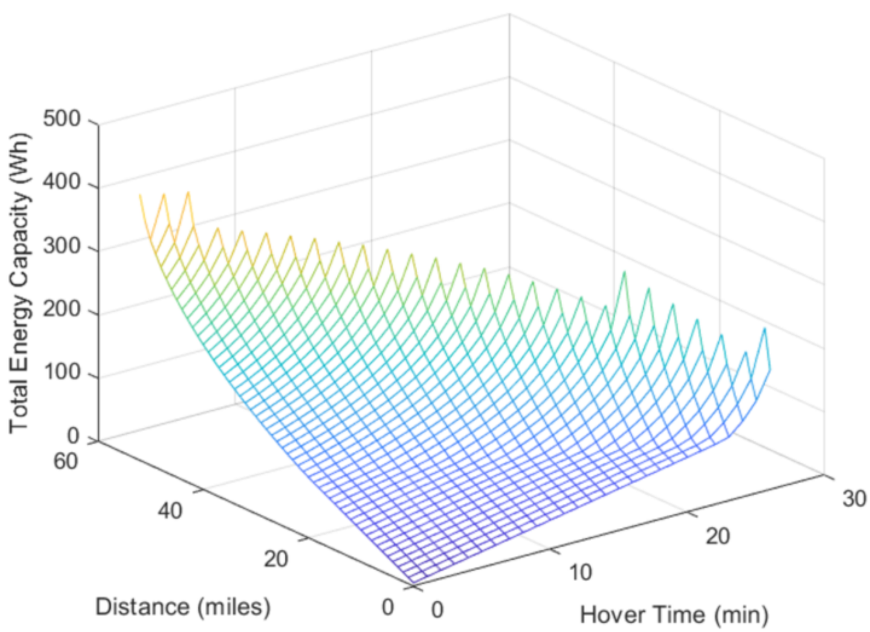

Figure 6.8: Total energy capacity based on mission for 2-prop thrust vectoring vehicle.

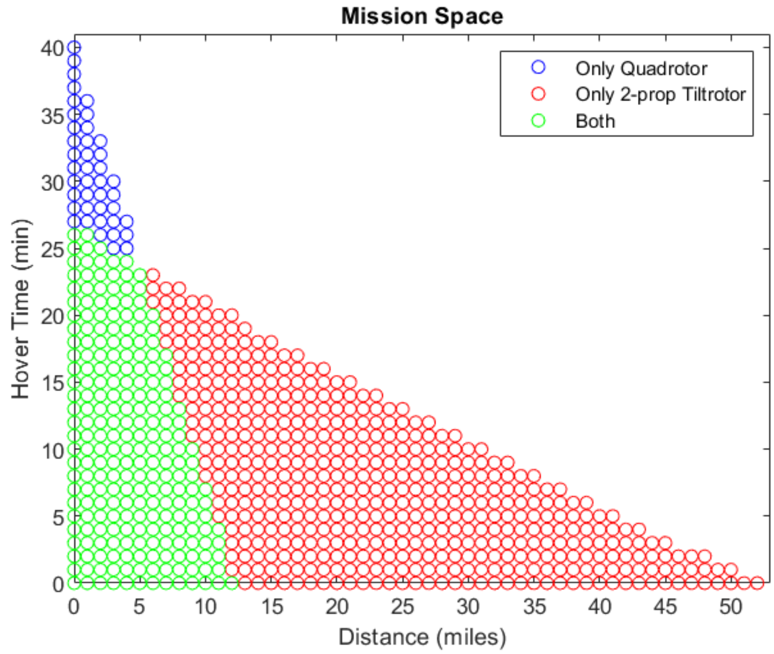

Figure 6.9: Mission space for sUAS quadrotors and 2-prop thrust vectoring vehicles.

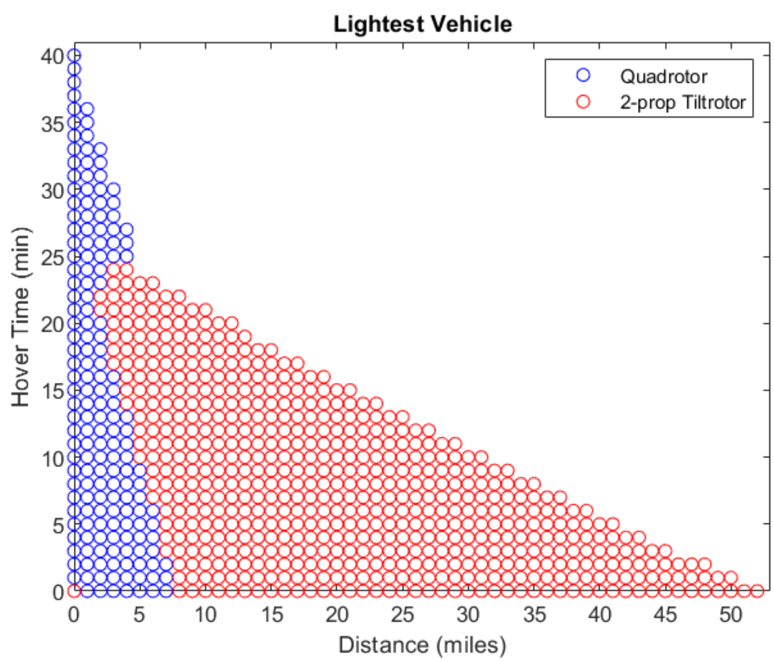

Figure 6.10: Lightest vehicle designed in mission space for sUAS quadrotor and 2-prop thrust vectoring vehicle.

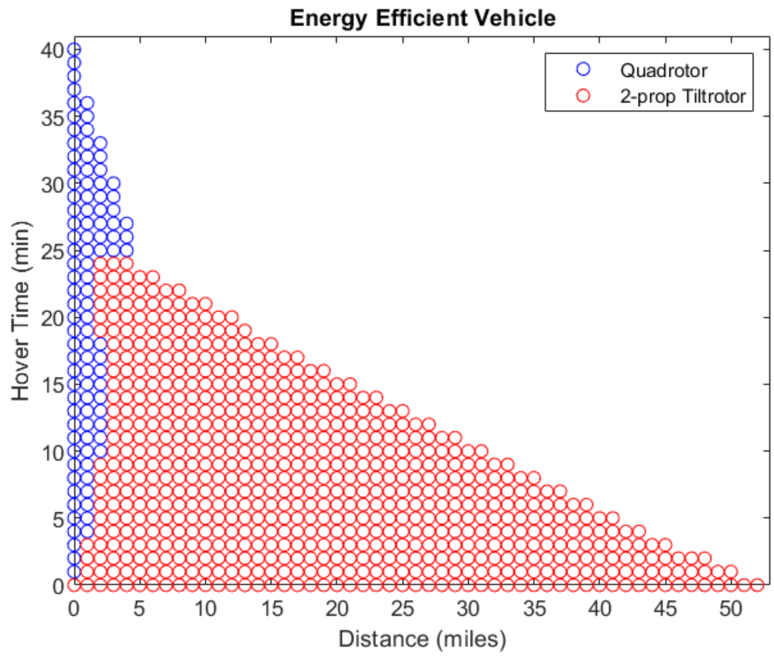

Figure 6.11: Least total energy capacity used in mission space for sUAS quadrotor and 2-prop thrust vectoring vehicle.

6.2 Vehicle Results based on Design Methodology

A 2-prop thrust vectoring vehicle was conceptually designed using the validated design methodology and information gained from the mission space exploration. A mission of 10 minute hover and 5 mile cruise was selected, based on Figure 6.9, because it lands at the crossover section between the quadrotor and 2-prop thrust vectoring vehicles. Vehicle parameters designed are shown in Table 6.1. The predicted weights of individual components are shown in Table 6.2. For Table 6.2, the individual weights of the propeller, motor, and ESC are shown, however, there are 2 of each for this vehicle design. Lastly, the design results from the design methodology for a 2-prop thrust vectoring vehicle are shown to scale in Figure 6.12.

The design of a 2-prop thrust vectoring vehicle using this design methodology produces reasonable results. The result of this design methodology is a starting point to begin detailed design for vehicle fabrication. Using the designed vehicle parameters and predicted weights, one could fabricate a vehicle to complete the desired mission. The individual component design is reasonable as shown in Figure 6.12. Even though the 2-prop thrust vectoring vehicle design was shown in this thesis, other configurations can also be conceptually designed using this design methodology.

Table 6.1: Vehicle parameters from the design of 2-prop thrust vectoring vehicle.

Parameter	Designed Value
Airspeed (m/s)	16
Payload Weight (lbs)	0.25
Number of Motors	2
Number of Blades	3
Disk Loading ($^{lbs}/_{ft^2}$)	2.0
Fuselage Radius (in)	2
Fuselage Length (in)	20
Aspect Ratio	11
Taper Ratio	0.4
Wing Area (ft^2)	0.653
Wing Span (ft)	2.68
Average Chord (in)	2.93
Horizontal Stabilizer Tail Area (in^2)	12.55
Vertical Stabilizer Tail Area (in^2)	9.22
Aspect Ratio HT	3
Aspect Ratio VT	1.3
Quarter Chord of Wing to Tail Length (in)	13.33

Table 6.2: Predicted weight values for individual components for 2-prop thrust vectoring vehicle.

Component	Weight (lbs)
Propeller (individual)	0.014
Motor (individual)	0.067
ESC (individual)	0.018
Fuselage	0.205
Wing	0.081
Tail	0.012
Transition Mechanism	0.062
Avionics	0.228
Battery	1.250
Gross Vehicle	2.280

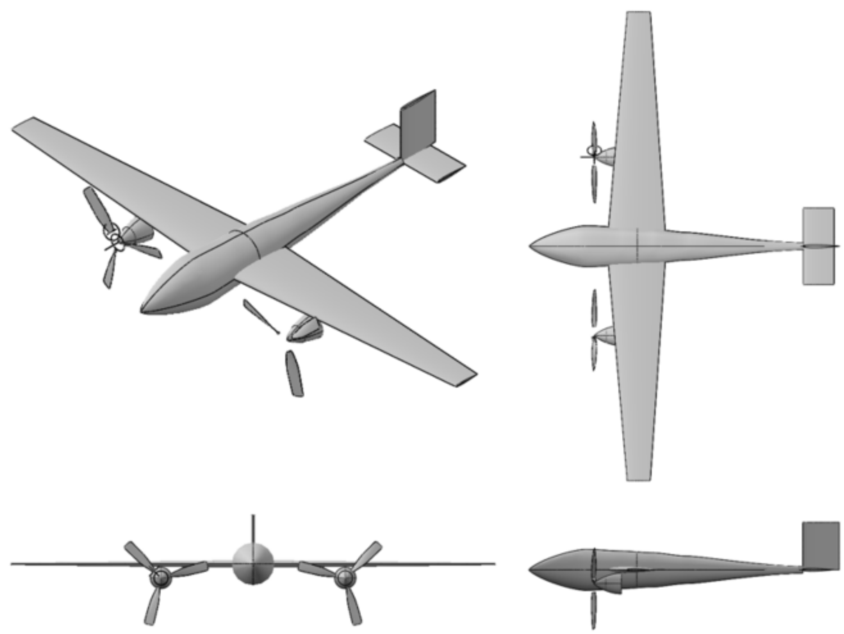

Figure 6.12: Isometric, top, left, and front views of 2-prop thrust vectoring vehicle design shown to scale.

Chapter 7 | Conclusions & Future Work

The objective of this thesis is to develop a validated design methodology for VTOL sUAS. This was accomplished by developing models for weight and aero-propulsive performance. These models were developed as component-based weight build-up, low-order drag build-up, momentum theory propeller model, and an empirical approach to motor-ESC efficiencies. These models were validated through flight testing of three VTOL sUAS in forward flight and hover. The following conclusions can be drawn from this process:

1. For the comparison to design models and flight test data, the developed method that was used to predict the power required in hover was within 13.1% of mean test data and the predicted power draw in forward flight was within 20.1% of mean test data. The empirical sub-component weight build-up approach predicted the total weight of the vehicles on average within 8.7%. The motor, ESC, and propeller efficiencies were found to be significantly lower than those previously assumed, resulting in a power required on the order of double the aero-propulsive power in forward flight. The drag was found to be dominated by the fuselage drag and generally sensitive to Reynolds number, as would be expected in the transitional flow region of operation. The assumed RPM of the propellers had a large influence on the predicted electric power results.
2. The validated models were integrated into an automated iterative design methodology that provided reasonable vehicle design results. This was shown through a conceptual design of a 2-prop thrust vectoring vehicle with a mission profile of 10 minute hover time and 5 mile cruise distance, which resulted in a vehicle gross weight of 2.28 pounds.
3. The mission space exploration completed using the design methodology revealed that in the crossover space between a quadrotor and 2-prop thrust vectoring vehicle, there is a difference between the lightest vehicle and the most energy-efficient vehicle. This further emphasizes that vehicle design objectives can vary the resultant vehicle design.

Future work for this thesis includes fabrication and testing of the conceptually designed 2-prop thrust vectoring vehicle, more validating flight test data for the design models, and additional configurations into the mission space. The fabrication and testing of the designed vehicle can provide validation for the developed design methodology within this scale of vehicles. The inclusion of more validation data for the design models involves additional vehicles and different configurations, which can provide additional validity to the current design models. The inclusion of additional configurations into the mission space will allow more trends of the VTOL sUAS configuration design space to be revealed. Additional future work is increasing the range of vehicle scale that is validated and includes different types of missions than just hover and forward flight.

Bibliography

[1] Federal Aviation Administration, "Part 107 Small Unmanned Aircraft Systems," , Jun. 2016. URL `https://www.ecfr.gov/current/title-14/part-107`.

[2] UAS Task Force, "Unmanned Aircraft System Airspace Integration Plan," Tech. rep., U.S. Department of Defense, 2011.

[3] Gundlach, J., *Designing Unmanned Aircraft Systems – A Comprehensive Approach*, American Institute of Aeronautics and Astronautics (AIAA), 2012.

[4] Ozdemir, U., Aktas, Y. O., Vuruskan, A., Dereli, Y., Tarhan, A. F., Demirbag, K., Erdem, A., Kalaycioglu, G. D., Ozkol, I., and Inalhan, G., "Design of a Commercial Hybrid VTOL UAV System," *Journal of Intelligent & Robotic Systems*, 2014. doi:`10.1007/s10846-013-9900-0`.

[5] Priyambodo, T., Majid, A., and Shouran, Z., "Validation of Quad Tail-sitter VTOL UAV Model in Fixed Wing Mode," *Journal of Robotics and Control (JRC)*, 2023. doi:`10.18196/jrc.v4i2.17253`.

[6] Chipade, V. S., Abhishek, Kothari, M., and Chaudhari, R. R., "Systematic design methodology for development and flight testing of a variable pitch quadrotor biplane VTOL UAV for payload delivery," *Mechatronics*, 2018. doi:`10.1016/j.mechatronics.2018.08.008`.

[7] Qin, Y., Xu, W., Lee, A., and Zhang, F., "Gemini: A Compact Yet Efficient Bi-Copter UAV for Indoor Applications," *IEEE Robotics and Automation Letters*, 2020. doi:`10.1109/LRA.2020.2974718`.

[8] Wang, Y., Lyu, X., Gu, H., Shen, S., Li, Z., and Zhang, F., "Design, implementation and verification of a quadrotor tail-sitter VTOL UAV," *2017 International Conference on Unmanned Aircraft Systems (ICUAS)*, 2017. doi:`10.1109/ICUAS.2017.7991419`.

[9] Dündar, O., Bilici, M., and Ünler, T., "Design and performance analyses of a fixed wing battery VTOL UAV," *Engineering Science and Technology, an International Journal*, 2020. doi:`10.1016/j.jestch.2020.02.002`.

[10] Lyu, C., Lu, D., Xiong, C., Hu, R., Jin, Y., Wang, J., Zeng, Z., and Lian, L., "Toward a gliding hybrid aerial underwater vehicle: Design, fabrication, and experiments," *Journal of Field Robotics*, 2022. doi:`10.1002/rob.22063`.

[11] Palaia, G., Abu Salem, K., Cipolla, V., Binante, V., and Zanetti, D., “A Conceptual Design Methodology for e-VTOL Aircraft for Urban Air Mobility,” *Applied Sciences*, 2021. doi:10.3390/app112210815.

[12] Ke, Y., Wang, K., and Chen, B. M., “Design and Implementation of a Hybrid UAV With Model-Based Flight Capabilities,” *IEEE/ASME Transactions on Mechatronics*, 2018. doi:10.1109/TMECH.2018.2820222.

[13] Kubo, D., and Suzuki, S., “Tail-Sitter Vertical Takeoff and Landing Unmanned Aerial Vehicle: Transitional Flight Analysis,” *Journal of Aircraft*, 2008. doi:10.2514/1.30122.

[14] Bacchini, A., and Cestino, E., “Electric VTOL Configurations Comparison,” *Aerospace*, 2019. doi:10.3390/aerospace6030026.

[15] Partovi, A. R., Zong Yao Kevin, A., Lin, H., Chen, B., and Cai, G., “Development of a Cross Style Quadrotor,” *AIAA Guidance, Navigation, and Control Conference*, American Institute of Aeronautics and Astronautics, 2012. doi:10.2514/6.2012-4780.

[16] Bershadsky, D., “Electric Multirotor Design and Optimization,” Ph.D. thesis, Geogia Tech University, Jul. 2017.

[17] Hendrix, S. G., Kenny, V., You, S., Khilnani, A., Dai, R., and Rea, J. R., “Experimental Testing for a Learning-based Powered-Descent Guidance Algorithm,” *AIAA SCITECH 2022 Forum*, American Institute of Aeronautics and Astronautics, 2021. doi:10.2514/6.2022-0952.

[18] Gu, H., Lyu, X., Li, Z., Shen, S., and Zhang, F., “Development and experimental verification of a hybrid vertical take-off and landing (VTOL) unmanned aerial vehicle (UAV),” *2017 International Conference on Unmanned Aircraft Systems (ICUAS)*, 2017. doi:10.1109/ICUAS.2017.7991420.

[19] Wang, B., Hou, Z., Liu, Z., Chen, Q., and Zhu, X., “Preliminary Design of a Small Unmanned Battery Powered Tailsitter,” *International Journal of Aerospace Engineering*, 2016. doi:10.1155/2016/3570581.

[20] Schaefer, C., and Baskett, L., “GoldenEye: The Clandestine UAV,” *2nd AIAA "Unmanned Unlimited" Conf. and Workshop & Exhibit*, American Institute of Aeronautics and Astronautics, 2003. doi:10.2514/6.2003-6634.

[21] Sanchez-Rivera, L. M., Lozano, R., and Arias-Montano, A., “Development, Modeling and Control of a Dual Tilt-Wing UAV in Vertical Flight,” *Drones*, 2020. doi:10.3390/drones4040071.

[22] Kim, J., and Choi, D., “Design and Control of a Novel Tiltrotor Platform,” *AIAA Infotech @ Aerospace*, AIAA SciTech Forum, American Institute of Aeronautics and Astronautics, 2016. doi:10.2514/6.2016-1254.

[23] Kamal, A., and Ramirez-Serrano, A., "Development of a Preliminary Design Methodology for Transitional UAV," *2018 AIAA Aerospace Sciences Meeting*, 2018. doi:10.2514/6.2018-1006.

[24] Axten, R. M., Khamvilai, T., and Johnson, E., "Multi-Outer Loop Adaptive Control for a VTOL Free-Wing Aircraft," *AIAA SCITECH 2024 Forum*, American Institute of Aeronautics and Astronautics, 2024. doi:10.2514/6.2024-0726.

[25] Bento, H. F., de Vries, R., and Veldhuis, L. L., "Aerodynamic Performance and Interaction Effects of Circular and Square Ducted Propellers," *AIAA Scitech 2020 Forum*, American Institute of Aeronautics and Astronautics, 2020. doi:10.2514/6.2020-1029.

[26] An, J.-H., Kwon, D.-Y., Jeon, K.-S., Tyan, M., and Lee, J.-W., "Advanced Sizing Methodology for a Multi-Mode eVTOL UAV Powered by a Hydrogen Fuel Cell and Battery," *Aerospace*, 2022. doi:10.3390/aerospace9020071.

[27] Keith, J., and Hall, D., "Rapid Sizing Methodologies for VTOL UAVs," *47th AIAA Aerospace Sciences Meeting including The New Horizons Forum and Aerospace Exposition*, 2009. doi:10.2514/6.2009-1617.

[28] Kadhiresan, A. R., and Duffy, M. J., "Conceptual Design and Mission Analysis for eVTOL Urban Air Mobility Flight Vehicle Configurations," *AIAA Aviation 2019 Forum*, 2019. doi:10.2514/6.2019-2873.

[29] Cole, J. A., Rajauski, L., Loughran, A., Karpowicz, A., and Salinger, S., "Configuration Study of Electric Helicopters for Urban Air Mobility," *Aerospace*, 2021. doi:10.3390/aerospace8020054.

[30] Babetto, L., and Stumpf, E., "Recent Development of a Conceptual Design Methodology for Unmanned Aerial Vehicles," *AIAA AVIATION 2021 Forum*, 2021. doi:10.2514/6.2021-3219.

[31] Russell, C. R., Theodore, C. R., and Sekula, M. K., "Incorporating Test Data for Small UAS at the Conceptual Design Level," *NASA Technical Report*, 2018.

[32] NDARC, "NASA Design and Analysis of Rotorcraft," https://rotorcraft.arc.nasa.gov/ndarc/, 2023.

[33] Topper, E., "Calibration and Validation of a Rotorcraft Design and Anaylsis Tool for Electric Powered Multirotor Configurations," Master's thesis, The Pennslyviannia State University, 2022.

[34] Daejin, L., Hyeongseok, K., and Kwanjung, Y., "Mission-oriented performance assessment and optimization of electric multirotors," *Aerospace Science and Technology*, 2021.

[35] Pollet, F., Delbecq, S., Budinger, M., Moschetta, J.-M., and Liscouët, J., "A common framework for the design optimization of fixed-wing, multicopter and VTOL UAV configurations," *33rd Congress of the International Council of the Aeronautical Sciences*, 2022. URL https://hal.science/hal-03832115.

[36] Gong, A., and Verstraete, D., "Experimental Testing of Electronic Speed Controllers for UAVs," *53rd AIAA/SAE/ASEE Joint Propulsion Conference*, 2017. doi:10.2514/6.2017-4955.

[37] Green, C. R., and McDonald, R. A., "Modeling and Test of the Efficiency of Electronic Speed Controllers for Brushless DC Motors," *15th AIAA Aviation Technology, Integration, and Operations Conference*, 2015. doi:10.2514/6.2015-3191.

[38] Ol, M., Zeune, C., and Logan, M., "Analytical/Experimental Comparison for Small Electric Unmanned Air Vehicle Propellers," *26th AIAA Applied Aerodynamics Conference*, American Institute of Aeronautics and Astronautics, 2008. doi:10.2514/6.2008-7345.

[39] Il-hyoung, L., Dong-jin, L., and Hyochoong, B., "A Small Scale Rotor UAV Autonomous Flight Control System Design and Verification," *AIAA Infotech Aerospace*, 2007.

[40] Loughran, A. P., Jones, T., Miller, S., and Cole, J., "Design Model Validation for Small UAS VTOL using Flight Test Data," *AIAA SCITECH 2024 Forum*, American Institute of Aeronautics and Astronautics, 2024. doi:10.2514/6.2024-2645.

[41] Leishman, J. G., *Principles of Helicopter Aerodynamics*, 2nd ed., Cambridge University Press Cambridge, 2006.

[42] Johnson, W., *Helicopter Theory*, Dover Publications, 1980.

[43] Drela, M., and Youngren, H., "XFOIL Subsonic Airfoil Development System," *MIT*, 2001.

[44] Hoerner, S. F., "Fluid-Dynamic Drag," *Chapter V-Drag of Surface Imperfections*, 1958.

[45] Anderson Jr., J. D., *Fundamentals of Aerodynamics*, 6th ed., McGraw-Hill Education, 2017.

[46] Götten, F., Havermann, M., Braun, C., Marino, M., and Bil, C., "Improved Form Factor for Drag Estimation of Fuselages with Various Cross Sections," *Journal of Aircraft*, 2021. doi:10.2514/1.C036032.

[47] McCormick, B. W., *Aerodynamics, Aeronautics, and Flight Mechanics*, 2nd ed., Wiley, 1995.

[48] Carroll, T., George, I.-R. E., and Bramesfeld, G., "Design Optimization of Small Rotors in Quad-Rotor Configuration," *54th AIAA Aerospace Sciences Meeting*, AIAA SciTech Forum, American Institute of Aeronautics and Astronautics, 2016. doi:10.2514/6.2016-1788.

[49] Tyto Robotics, "Propellers List," https://database.tytorobotics.com/propellers, 2023. Accessed: 2023 December 5.

[50] Nagel, L., "A Guide to Lithium Polymer Batteries for Drones," https://www.tytorobotics.com/blogs/articles/a-guide-to-lithium-polymer-batteries-for-drones, 2023. Accessed: 2023 September 26.

[51] Aircraft Spruce, "Last-A-Foam 4.5 1/2X24X48," https://www.aircraftspruce.com/catalog/cmpages/lastafoam.php, 2023. Accessed: 2023 September 26.

[52] McAlister, K. W., and Takahashi, R. K., "NACA 0015 Wing Pressure and Trailing Vortex Measurements," Tech. rep., NASA, 1991.

[53] Blouin, C., "How to Measure Brushless Motor and Propeller Efficiency," , 2022. URL https://www.tytorobotics.com/blogs/articles/how-to-measure-brushless-motor-and-propeller-efficiency.

[54] HEEWING, "T1 Ranger — Kit," https://www.heewing.com/products/t1-ranger-kit, 2023. Accessed: 2023 November 28.

[55] ARRISHOBBY, "Jumper XiaKe 800 Portable Fixed Wing VTOL Wingspan 800mm FPV Aircraft Long Flight Airplanes," https://www.arrishobby.com/products/jumper-xiake-800-portable-fixed-wing-y3-vertical-takeoff-wingspan-800mm-fpv-aircraft-long-flight-airplanes, 2023. Accessed: 2023 November 28.

[56] Flite Test Retail Store, "FT Bronco MKR2," https://store.flitetest.com/ft-bronco-mkr2, 2023. Accessed: 2023 November 28.

[57] ArduPilot, "ArduPilot - Versatile, Trusted, Open," https://ardupilot.org, 2023. Accessed: 2023 October 5.

[58] "Pixhawk Overview — Copter documentation," , 2023. URL https://ardupilot.org/copter/docs/common-pixhawk-overview.html.

[59] Computational Fluid Dynamics Committee, "Guide for the Verification and Validation of Computational Fluid Dynamics Simulations (AIAA G-077-1998(2002))," *AIAA Standards*, American Institute of Aeronautics and Astronautics, Inc., 1998. doi:10.2514/4.472855.001.

[60] "V40*16-Prop-2PCS/PAIR," , 2023. URL https://store.tmotor.com/goods-888-V40%2A16-Prop-2PCSPAIR.html, accessed: 2023 September 26.

[61] "Flywoo 1609 4-Blade 1.5mm Shaft 40mm Propellers (Set of 8) - Clear Black," , 2024. URL https://www.getfpv.com/flywoo-1609-4-blade-1-5mm-shaft-40mm-propellers-set-of-8-clear-black.html, accessed: 2024 February 14.

[62] Kee, S. G., "Guide for conceptual helicopter design," Master's thesis, Naval Postgraduate School, 1983. URL http://archive.org/details/guideforconceptu1094519825.

[63] Raymer, D., *Aircraft Design: A Conceptual Approach*, 5th ed., American Institute of Aeronautics and Astronautics, 2012.

[64] Bershadsky, D., Haviland, S., and Johnson, E. N., "Electric Multirotor UAV Propulsion System Sizing for Performance Prediction and Design Optimization," *57th AIAA/ASCE/AHS/ASC Structures, Structural Dynamics, and Materials Conference*, AIAA SciTech Forum, American Institute of Aeronautics and Astronautics, 2016. doi:10.2514/6.2016-0581.

[65] McDonald, R., "Batteries are not Fuel," https://www.linkedin.com/pulse/batteries-fuel-rob-mcdonald, 2023.

[66] PSU ATSV, "ARL Trade Space Exploration," http://www.atsv.psu.edu, 2010.